Spatial transcriptomics elucidates medulla niche supporting germinal center response in myasthenia gravis thymoma

Authors

Yoshiaki Yasumizu[1,2,3,12,*], Makoto Kinoshita[1], Martin Jinye Zhang[4,5], Daisuke Motooka[3,6], Koichiro Suzuki[7,8], Daisuke Okuzaki[3,6], Satoshi Nojima[9], Soichiro Funaki[10], Yasushi Shintani[10], Naganari Ohkura[2,11], Eiichi Morii[9], Tatsusada Okuno[1,*], Hideki Mochizuki[1,3]

1. Department of Neurology, Graduate School of Medicine, Osaka University, Suita, Osaka, Japan
2. Department of Experimental Immunology, Immunology Frontier Research Center, Osaka University, Suita, Osaka, Japan
3. Integrated Frontier Research for Medical Science Division, Institute for Open and Transdisciplinary Research Initiatives (OTRI), Osaka University, Suita, Osaka, Japan
4. Ray and Stephanie Lane Computational Biology Department, School of Computer Science, Carnegie Mellon University, Pittsburgh, PA, USA
5. Department of Epidemiology, Harvard T.H. Chan School of Public Health, Boston, MA, USA
6. Genome Information Research Center, Research Institute for Microbial Diseases, Osaka University, Suita, Osaka, Japan
7. BIKEN-RIMD NGS Laboratory, Research Institute for Microbial Diseases, Osaka University, Suita, Japan
8. Biomedical Science Center, The Research Foundation for Microbial Diseases of Osaka University (BIKEN), Suita, Japan
9. Department of Pathology, Graduate School of Medicine, Osaka University, Suita, Osaka, Japan
10. Department of General Thoracic Surgery, Graduate School of Medicine, Osaka University, Suita, Osaka, Japan
11. Department of Frontier Research in Tumor Immunology, Graduate School of Medicine, Osaka University, Suita, Osaka, Japan
12. Lead Contact

* Correspondence

Correspondence:

Yoshiaki Yasumizu: yyasumizu@ifrec.osaka-u.ac.jp

Tatsusada Okuno: okuno@neurol.med.osaka-u.ac.jp

Summary

Myasthenia gravis (MG) is known to be epidemiologically associated with abnormalities of the thymus, an organ that maintains central tolerance. However, due to the complexity of the thymus, specific characteristics related to the pathogenesis of MG remain elusive. In our study, we attempted to narrow down the features associated with MG using spatial transcriptome analysis of thymoma and thymic hyperplasia samples. We found that the majority of thymomas were constituted by the cortical region, whereas the medullary region was localized in comparatively restricted areas. Moreover, the medullary region contained polygenic enrichment, MG-specific germinal center structures, and a supporting immune microenvironment. Additionally, neuromuscular medullary thymic epithelial cells (nmTECs), previously identified as MG-specific autoantigen-producing cells, were situated at the cortico-medullary junction. The immune microenvironment in the medulla was characterized by a specific chemokine pattern and specific immune cells, such as *CCR7*$^+$ migratory dendritic cells (migDCs) and effector regulatory T (Treg) cells. Furthermore, similar germinal center structures and immune microenvironments were observed in the medulla during thymic hyperplasia. This study indicates that the medulla and junction areas are related to the pathology of MG, suggesting that these areas should be the focus of future studies on MG pathogenesis and drug targeting.

Introduction

Myasthenia gravis (MG) is an autoimmune disease that causes systemic muscle weakness due to the production of autoantibodies that target the neuromuscular junction. Similar to other autoimmune diseases, genome-wide association studies (GWAS) have identified MG as a polygenic disease, with variants associated with T cell and B cell functions [1,2]. MG is also associated with thymoma and thymic hyperplasia. Currently, a thymectomy is the first choice of treatment for MG with thymoma, and the effectiveness of this treatment underscores the role of the thymus in disease pathogenesis [3,4]. However, a thymectomy is an invasive surgical procedure that can adversely affect the immune system [5]. In addition to thymectomy, only symptomatic treatments targeting the immune system or neuromuscular junctions are available, underscoring the need for the development of novel, less-invasive treatments that act upstream of the disease pathway. Therefore, the identification of thymic abnormalities related to MG is urgently needed.

The thymus is the primary lymphoid organ responsible for T cell education; it eliminates autoreactive T cells and induces regulatory T cells (Tregs), which serve as the site of central tolerance. However, due to the complexity of thymic function and anatomy, its physiological role and involvement in MG remain unclear. We previously identified the abnormal expression of neuromuscular-related antigen molecules in MG-specific medullary thymic epithelial cells (mTECs) and germinal center (GC) formation in MG-associated thymomas using single-cell RNA sequencing (scRNA-seq) analysis [6]. However, spatial interpretation using scRNA-seq remains challenging. Therefore, there has been no spatial prioritization to determine the areas within the complex thymic tissue that are truly related to the disease thus far. Although our scRNA-seq results suggested interactions between mTECs and immune cells, their spatial proximity was not confirmed. Furthermore, a comprehensive understanding of the immune cells that form niches within the thymus is lacking.

Additionally, MG is associated not only with thymomas but also with thymic hyperplasia in younger patients [7]. Thymic hyperplasia is a benign condition characterized by the enlargement of the normal thymus and, similar to thymomas, is reported to involve the formation of lymphoid follicles with GCs [8]. Although both thymomas and thymic hyperplasia are thymic abnormalities associated with MG, whether there is a pathogenic link between the two remains controversial.

In recent years, spatial transcriptomics technology has evolved, greatly advancing our spatial understanding of disease analysis [9–11]. Spatial transcriptomics has enabled significant improvements in the interpretation of cellular niches compared to observational methods with fewer parameters, such as hematoxylin and eosin (H&E) staining or immunohistochemistry. However, despite the significant amount of information it provides, assigning pathological significance and considering causality using spatial transcriptomics alone has been challenging. By integrating scRNA-seq data from the corresponding tissue, we can extract more information and estimate the cellular composition of each spot for a more detailed interpretation [12]. Nonetheless, there is currently no consensus on how to appropriately prioritize susceptible regions.

In this study, we conducted a spatial evaluation of MG thymomas using spatial transcriptome analysis to identify disease-related niches and characterize distinctive gene expression. We developed a new method, single-cell disease-relevance score (scDRS)-spatial, which leverages polygenic enrichment to identify disease-relevant spatial locations by integrating single-cell spatial transcriptomics with disease GWAS, extending an existing method, scDRS [13], that analyzes scRNA-seq data. In particular, scDRS-spatial considers physical contact between multiple cells, in addition to cell type-specific polygenic enrichment, by assessing spatial niches rather than single cells. Furthermore, we reconstructed the largest single-cell atlas of thymomas by integrating data from previous reports [6,14]. By integrating this atlas with spatial transcriptomic data, we were able to estimate the detailed spatial interactions between cell populations. Through these integrated analyses, we attempted to identify hotspots of MG pathology in MG thymomas and the immune responses at these sites. Finally, we conducted a spatial transcriptome analysis of MG-associated thymic hyperplasia and discussed the similarities between the immune microenvironments of MG thymomas and hyperplasia.

Results

Spatial-transcriptome profiling of thymoma, hyperplasia, and normal thymus

To investigate the spatial characteristics of thymuses associated with MG, we conducted a spatial transcriptome analysis. We previously reported a stronger association between thymomas and the presence of anti-acetylcholine receptor antibodies (AChR-Abs) than with the presence of MG-related symptoms. In this study, we primarily profiled thymomas (the World Health Organization classification Type B1 or B2) in patients positive for AChR-Ab (seropositive) as MG-type thymomas. We profiled the thymomas of four seropositive patients, two of whom exhibited MG symptoms, yielding five samples. Additionally, three samples were obtained from three seronegative patients

(AChR-Ab-negative, WHO Type B1 or B2), and two thymic hyperplasia samples were obtained from two seropositive patients with MG symptoms. Formalin-fixed and paraffin-embedded sections were profiled using the 10x Visium platform (Figure 1A, Table S1). For comparison with normal thymuses, we integrated the Visium data of 11 samples from 11 individuals with normal fetal and pediatric thymuses. After quality control, 59,796 spots were retained for downstream analyses. Because each Visium spot is estimated to contain approximately 1-10 cells, each spot can be considered to represent a niche. Initially, the Leiden algorithm was used to define 18 clusters (Figures 1B, S1A, and B). Based on these 18 Leiden clusters, we defined six annotated clusters: the cortex, medulla, Junction, Stroma, and two medulla-specific clusters characterized by *FN1* expression (medulla_FN1) and a high concentration of GCs (medulla_GC) (Figures 1B,C). For instance, the distinct expression of chemokine-receptor pairs, such as *CCR9-CCL25* and *CCR7-CCL19,* significantly differentiated the cortex from the medulla (Figures 1D and S1C). The transcriptome profiles of the medulla and cortex were maintained, even in tumors (Figure 1D). Spatially, in normal thymuses, the cortex typically formed an outer layer with the medulla inside, whereas in thymomas, small medullary structures (on average, 9.77% in thymoma and 19.8% in normal thymus) were interspersed predominantly within cortical structures (on average, 80.6% in thymoma and 73.9% in normal thymus) (Figures S1B and S2), as previously suggested [15]. The junction area was positioned both transcriptomically and spatially between the medulla and cortex (Figures 1C and S1D-F). Examination of the regional proportions of thymomas between seropositive and seronegative cases revealed no significant differences at the Leiden cluster level. However, the cortical region exhibited a significant decrease in seropositive cases (Figures 1E-G and S1G). The expression of an MG-specific gene set (termed as “yellow module”) [6] was highest in the junction (Figures S1H,I). Thus, by clustering the spatial transcriptome data of the thymus, we identified the predominant cortical and interspersed medullary structures in thymomas and revealed a reduction in the proportion of the cortex in MG-associated thymomas.

Prioritization of pathogenic niche in MG thymoma

Similar to other autoimmune diseases, MG is polygenic. We hypothesized that identifying the niches with genetic susceptibility to MG accumulation would allow us to prioritize these niches (Figure

S3A). To this end, we extended scDRS [13] to spatial data, namely, the scDRS-spatial framework. scDRS integrates scRNA-seq data with GWAS to identify cell types with polygenic enrichment. scDRS-spatial goes beyond the cellular level by further assessing the polygenic enrichment of spatial niches that are hotspots of physical intercellular contact. First, we conducted null simulations using random gene sets and confirmed that scDRS-spatial was well calibrated for spatial transcriptome data (Figure S3B). Specifically, an imputation using Markov Affinity-based Graph Imputation of Cells (MAGIC) [16] produced conservative estimates (Figure S3B). Based on these findings, we imputed spatial data using MAGIC to reduce technical noise and estimated polygenic enrichment at each spot using scDRS-spatial. Furthermore, we added Visium data from various tissues across the human body as controls (Table S3). At the tissue level, the spots in the thymus were significantly associated with MG (Figure S3C). At the level of Leiden clusters, niche 8 (corresponding to the medulla) was significantly associated with a false discovery rate (FDR) of <0.2; Figure S3D). Across all regions, the medulla was significantly associated with MG (FDR<0.2; Figure S3E). Moreover, when stratified by condition, the proportion of associated niches and the heterogeneity in the medulla, especially niche 8, were higher in seropositive thymomas than in seronegative thymomas and the normal thymus (Figures 2A-C). These results suggest that genetic susceptibility accumulates in the medullary regions of thymomas.

Cellular composition in MG-thymoma niche

To elucidate the cellular composition of MG-thymoma niches, we performed cell deconvolution by integrating scRNA-seq data. For deconvolution, we created a new single-cell reference for thymomas by adding our data to the single-cell data reported by Xin *et al.* [14]. After quality control, 113,948 cells were retained, defining 50 clusters, including immune, epithelial, and stromal cells (Figures 3A,B and S4A-F). Notably, we achieved a higher-precision annotation of the TEC population, which was less represented in our previous study [6]. The medullary TECs (mTECs) were characterized by the expression of *CLDN4* (Figure S4A). Within the mTECs, several sub-clusters were defined, including *AIRE*^{high} mTECs (mTEC *AIRE*), *KRT14*^{high} mTECs (mTEC *KRT14*), and neuromuscular mTECs (nmTECs), which were characterized by a high yellow module and *GABRA5* expression (Figure S4B). The DC fraction also included plasmacytoid DCs (pDC), conventional DCs type 1 (cDC1), type 2 (cDC2), and migDCs, which were characterized by *CCR7* and *LAMP3* expression. MigDCs expressed both *CD274* (PD-L1) and *CD80*, suggesting the involvement of T cell activation [17] (Figure S4G). We then assessed MG-specific features in the new references to confirm their consistency. Deconvolution using bulk RNA-seq data of thymomas generated by The Cancer Genome Atlas (TCGA) [18] consortium revealed that the frequency of nmTECs was the most significantly associated with MG (Figure S5A, padj= 6×10^{-6}), similar to a previous result [6]. In addition, the expression of yellow module genes was highest in nmTECs (Figure S5B). This observation indicates that nmTECs were the most associated cell type at the single-cell level, even in the new single-cell reference, which elaborated on the TEC populations.

Next, we leveraged a new single-cell reference to analyze the spatial transcriptome data at cell-type resolution. By integrating the single-cell reference with Visium data using cell2location [12], we estimated the cellular composition of each spot (Figures 3C,D). As in the normal thymus, immature T cells, such as $CD4^-$ $CD8^-$ double-negative cells and $CD4^+$ $CD8^+$ double-positive T cells, were concentrated in the cortical region, whereas mature T cells and mTECs were abundant in the medullary region (Figures 3C,D). Germinal center B cells (B GC) and *CXCL13*-producing T follicular helper cells (CD4 Tfh *CXCL13*) were also enriched in the medullary GC region (Figures 3C,D). The stroma and medulla_FN1 regions were characterized by high numbers of endothelial cells, fibroblasts, and vascular smooth muscle cells (VSMCs) (Figures 3C,S6A). In the seropositive cases, an increase in nmTECs, immune cells, such as antigen-secreting cells (ASC), switched memory B cells (B SM), B GC, migDCs, and effector T regulatory cells (Treg Eff), and reduced cTECs were confirmed (Figures 3E and S6B). Next, we explored the co-localization patterns of constituent cells using non-negative matrix factorization (NMF), defining eight co-localization factors (factors 0–7) (Figures 3F-H,S6C). By analyzing the cellular contributions and enriched regions of each factor, we found that certain factors were predominantly associated with specific regions: factors 0, 2, and 4 with the cortex, factor 5 with the medulla, factors 1 and 3 with the stroma, and factor 7 with both the junction and GCs. Factor 7, composed of B GC, was localized within GCs, while CD4 Tfh *CXCL13* was present both inside and around GCs in the medullary region, forming the GC niche (Figures 3F-H,S6C). Factor 5, composed of mature immune cells, such as Treg Eff, migDCs, and B SM, constituted an immune microenvironment in the medulla (Figures 3F-H,S6C). Factor 6, comprising nmTECs, cDC1, and migDCs, was particularly abundant at the junction area (Figures 3F-H,S6C). The ASC niche was not identified within the cortex or medulla but was present in the stromal region (Figures 3C,S6A). Endothelial cells were concentrated in the medulla and stroma, highlighting a lower vascular presence in the cortex (Figures 3C,S6A). In summary, cell deconvolution identified eight co-localizing communities and their constituent cells.

Cell-cell interaction analysis reveals niche-specific chemokine profiles

Next, we analyzed cell-cell interactions (CCIs) within the cell groups constituting the niches. Using CellphoneDB [19], we explored CCIs by considering the co-localizing communities identified by cell2location analysis. Numerous CCIs were identified, among which chemokines were particularly cell-specific and appeared to be involved in niche-specific cell migration (Figure S7A,B). In both tumor and normal tissues, *CCL25*-*CCR9* and *CCL19*-*CCR7* interactions were specific to the cortex and medulla, respectively (Figures 4A,B). Previously, we reported that nmTECs have an intermediate profile between that of mTECs and cTECs [6], and indeed, they expressed both *CCL25* and *CCL19* (Figure 4A). Interestingly, in thymomas, both single-positive T cells and migratory DCs (migDCs) expressed *CCR7*, suggesting that the medullary characteristics of thymomas facilitate the mobilization of migDCs. Ligands for *CCR4* specific to Treg Eff, such as *CCL17* and *CCL22*, were expressed by migDCs in thymomas, suggesting their role in maintaining Treg Eff in the medulla [20] (Figures 4A,B). Similarly, *CXCL16*, the ligand for *CXCR6* specific to Treg Eff, was expressed in cDC1, cDC2, and migDCs (Figures 4A,B). MigDCs also expressed *CXCL10*, which potentially interacts with *CXCR3*$^+$ effector T cells (Figures 4A,B). We previously demonstrated that mature infiltrating T/B cells in the thymus specifically express *CXCR4* [6]. The *CXCL12* ligand was expressed by nmTECs [6], suggesting its role in maintaining the medullary niche (Figures 4A,B). Finally, *CXCL13,* a key chemokine for the maintenance of the GC, was expressed by CD4 Tfh *CXCL13* (Figure 4A). The expression of *CCR4*, *CXCL16*, and *CXCR5*-*CXCL13* was lower in the normal thymus than in the thymoma, suggesting their thymoma-specific roles in maintaining niches (Figure 4A). In contrast, chemokines such as *CCL25*, *CCL19*, *CXCL12* and their receptors were expressed in both the normal thymus and thymoma, suggesting that some factors might be synchronized with normal conditions and MG thymoma (Figure 4A). Taken together, we identified spatially characteristic chemokine ligand-receptor pairs in thymomas, supporting the involvement of these niches in the pathogenesis of thymoma-associated MG.

Extrapolation of thymoma niche to thymic hyperplasia

Finally, we verified whether our findings were consistent with those in thymic hyperplasia. Anatomically similar to the normal thymus, the structure with the cortex on the outside and the medulla on the inside was maintained (Figure 5A). GCs are present in the medulla, similar to thymomas, suggesting that the microenvironment supporting GC formation is common in both thymomas and thymic hyperplasia. (Figure 5A). Polygenic signals identified by scDRS-spatial analysis were generally more enriched in thymoma samples and were particularly observed in the medulla, similar to our findings in thymomas (Figures 5B,C, S9A,B). Although there is no single-cell RNA-seq reference for thymic hyperplasia, application of the thymoma reference revealed that the eight-cell communities identified in thymomas were consistently formed in accordance with anatomical features (Figure 5D). Furthermore, the expression of chemokines and their receptors was consistent with thymomas, and *CCR4*, *CXCL16*, and *CXCR5-CXCL13*, which had lower expressions in the normal thymus, were abundantly expressed in hyperplasia (Figures 5E,F). These findings indicate that an immune microenvironment supporting GCs is present in the medulla in thymic hyperplasia, which is similar to thymoma.

Discussion

In this study, spatial transcriptomics was used to identify the niche involved in the pathogenesis of MG thymoma and to explore its molecular characteristics. We successfully identified the MG-associated niche and its constituents in both thymomas and thymic hyperplasia (Figure 6). Our analysis revealed that cortical-like areas, medullary-like areas, and immune hotspots coexisted within a single patient, highlighting the heterogeneity of the tumor environment within an individual. Genetic and phenotypic associations of the medulla were also suggested. Furthermore, we identified the formation of ectopic lymphoid structures (ELS) in the MG thymus and the chemokines that support these structures.

The significance of the medulla has been frequently discussed, including in our previous single-cell analyses [6,21–23]. mTECs play a crucial role in negative selection by eliminating autoreactive T cells through self-antigen production [24–26]. The abnormalities in this process in MG highlight that negative selection has a potential risk of inducing autoimmunity. In particular, the expression of neuromuscular-related antigens by nmTECs in MG thymomas has been suggested to feed on autoreactive T cells [6]. These nmTECs were localized at the junction of the medulla and cortex, suggesting that the origin of these nmTECs in tumor development was at this junction. Additionally, our analysis demonstrated the accumulation of migDCs in the medulla. MigDCs expressing *CCR7* migrate to tertiary lymphoid structures or lymph nodes with high concentrations of *CCL19* and play an important role in T cell priming [27,28]. The medulla, due to mTEC-induced *CCL19* expression, may physiologically trap migDCs and mediate T-cell help. Furthermore, CCI between migDCs and mTECs has been noted, even in the normal thymus [23], and this collaboration may be attributed to normal thymic function.

Furthermore, our analysis provides new insights into the role of specific immune cells in the pathogenesis of MG. A concurrent abundance of *CXCL13*$^+$ *IL21*$^+$ Tfh cells within the lymphoid follicles and accumulation of migDCs in the medulla were observed. These findings suggest that follicle formation in the thymus induces potent affinity maturation and B-cell proliferation, possibly contributing to the pathogenesis of MG [29,30]. However, *CXCR5*$^-$ *PDCD1*$^+$ T peripheral helper (Tph) cells, observed at inflammatory sites in rheumatoid arthritis, systemic lupus erythematosus, and Sjögren's syndrome [31–33], were not clearly identified as distinct cell populations in our single-cell analysis. While our study and others have reported an increase in circulating Tph cells in MG, these results were contrary to our expectation [2,34]. Additionally, effector Tregs were also observed to be abundant in the medulla of MG thymoma. Although the accumulation of GWAS signals in Tregs [2,6] and their dysfunction in MG patients [35] have been suggested, whether normalizing their function could lead to therapeutic effects remains an important question for future research.

Notably, as MG is an antibody-mediated disease, it has been reported that ASCs are increased in MG thymoma [36]. However, the niche for ASCs was not found within the thymic cortex or medulla but was rather abundant in the stromal region. Even after thymectomy, the circulation of autoreactive B-cell clones in the periphery has been reported [37], suggesting that extrathymic niches, such as the bone marrow [38], may harbor ASCs. Nevertheless, it was suggested that the immune microenvironment within the medulla primarily contributes to B cell maturation.

This study also profiled MG-associated thymic hyperplasia. Because there are no single-cell datasets specific to thymic hyperplasia, a detailed comparison of thymic epithelial cell profiles was not possible. Nonetheless, our analysis revealed notable similarities in immune cells, chemokine profiles, and polygenic signals in the medulla of MG thymomas. Consequently, this study offers an invaluable resource for understanding the pathogenesis of MG by presenting a comprehensive overview of thymomas and thymic hyperplasia.

In summary, using spatial transcriptomic analysis, we successfully identified the immune microenvironment in the medulla, revealing that many of its characteristics resonate with the physiological features of the thymus. Current treatments for MG, aside from thymectomy, are mainly supportive and target the immune system and neuromuscular junctions. We hope that this study will contribute to a complete understanding of MG pathogenesis and the development of novel treatments targeting upstream pathological processes.

STAR Methods

Human samples

This study was reviewed and approved by the Research Ethics Committee of Osaka University and was conducted in accordance with the guidelines and regulations. Human samples were collected with the approval of Osaka University's review board (protocol: ID 10038-13. Detailed information on the participants is provided in Table S1.

Spatial Transcriptomics (CytAssist Visium)

Formalin-fixed, paraffin-embedded (FFPE) thymoma samples were used. The samples were sliced into 8-μm-thick sections using a microtome. RNA quality was examined using DV200, and samples with DV200 > 25% were used for all subsequent analyses. Libraries were then constructed using the Visium workflow with CytAssist, according to the manufacturer's guidelines (CG000518, 10× Genomics, Pleasanton, CA, USA). Sequencing was performed at the Research Institute for Microbial Diseases, Osaka University. Libraries were sequenced using an MGI DNBSEQ-G400RS (MGI Tech Co., Shenzhen, China) system. The generated data were processed using Space Ranger v2.0.1 software, using GRCh38-2020-A as a reference.

Visium data analysis

For the assessment of normal thymus tissues, data from eight pediatric thymuses [39] and three fetal thymuses [40] were downloaded (GSE207205 and https://developmental.cellatlas.io/fetal-immune) and processed using Scanpy (1.9.5) [41]. Briefly, the data were loaded as anndata objects and concatenated. Spots classified as “in tissue” were retained. Thereafter, we performed normalization (sc.pp.normalize_total), log transformation (sc.pp.log1p) and extraction of HVGs (sc.pp.highly_variable_genes with the options, n_top_genes=3000, flavor='seurat_v3', batch_key='sample_id'). We then applied the variational inference model implemented in the scvi-tool (1.0.4) [42]. Sample IDs and Projects were specified as categorical covariates and total counts per cell were used as continuous covariates. The model (n_layers=2, n_latent=30) was trained using the default parameters and latent space for the UMAP embeddings and Leiden clustering using Scanpy. Marker genes were extracted using the scvi.model.differential_expression function. Gene scores were calculated using the sc.tl.score_genes function implemented in Scanpy with default parameters. Spatial neighborhood enrichment analysis was performed using the sq.gr.spatial_neighbors function implemented in Squidpy (1.3.1) [43]. Cell proportions were compared using the Bayesian framework implemented in scCODA [44]. The mixed effect model was implemented using the Python package, statsmodels (v0.14.0).

scDRS-spatial

The GWAS summary statistics deposited at GCST90093061 [1] were used for analysis. These summary statistics describe the meta-analysis results for MG. The cohort included 1,873 cases and 36,370 controls from the US and Italy, respectively. Gene scores were computed using MAGMA [45] (v1.10) software as described by Zhang *et al.* [13]. First, we performed single nucleotide polymorphism (SNP) annotation with gene locations (NCBI37.3, https://ctg.cncr.nl/software/MAGMA/aux_files/NCBI37.3.zip) and the reference data created from 1000 genomics Phase3 (g1000_eur, https://ctg.cncr.nl/software/MAGMA/ref_data/g1000_eur.zip) using magma --annotate (with the option, window=10,10). Next, we calculated the gene scores from the p-values using MAGMA. To include a variety of cell types in the dataset, we downloaded public Visium data (Table S3) and created a Visium control dataset. We then combined these with the thymus datasets. We pre-processed the dataset by normalizing the total counts to the median of the total counts (scanpy.pp.normalize_total), log transformation (scanpy.pp.log1p), and imputing gene expression using MAGIC [16] (scanpy.external.pp.magic). Thereafter, the polygenic enrichment for each cell was evaluated using scdrs compute-score (v1.0.3, options: --flag-filter-data True --flag-raw-count False --n-ctrl 1000); the number of genes for each cell was used as the covariate. Group-level statistics were calculated using scdrs perform-downstream and visualized using scdrs.util.plot_group_stats.

A null simulation was performed as described by Zhang *et al.* [13]. We randomly selected 1000 genes 100 times, and the enrichment for the Visium control dataset was evaluated using scdrs compute-score (--flag-filter-data True --flag-raw-count False --n-ctrl 1000 for imputed data, --flag-filter-data True --flag-raw-count True --n-ctrl 1000 for raw data).

Single-cell RNA-seq analysis

We pre-processed the scRNA-seq data of thymomas generated by Xin *et al.* [14]. First, doublets were removed using Scrublet [46] with default parameters, and cells with > 200 and < 8000 genes and < 20% mitochondrial RNA were retained. The data were then merged with the thymoma and PBMC datasets generated by Yasumizu *et al*. [6] To remove the effect of immune receptors on highly variable genes, genes related to T cell receptors and B cell receptors were removed. The retained expression was normalized (sc.pp.normalized_total with the option target_sum=1e4) and transformed (sc.pp.log1p), and highly variable genes were assessed (sc.pp.highly_variable_genes with the options flavor='seurat_v3', batch_key='project'). Cell cycle was inferred using the sc.tl.score_genes_cell_cycle function following a tutorial (https://nbviewer.jupyter.org/github/theislab/scanpy_usage/blob/master/180209_cell_cycle/cell_cycle.ipynb). The total UMI counts, percentage of mitochondrial genes, S score, and G2M score were regressed using sc.tl.regress_out and scaled using sc.tl.scale. The principal components were then computed using sc.tl.pca. The batch effect of the samples was eliminated using the Harmony algorithm [47]. Neighbors were calculated using sc.pp.neighbors with the options n_neighbors=30 n_pcs=50. Cells were embedded in UMAP using sc.tl.umap (spread = 2) and clustered using sc.tl.leiden. The initial layer clusters (cluster L1) were manually defined based on Leiden clusters. For Layer 2 clustering, we recursively extracted cells from a population and performed the same procedures with manually optimized parameters (number of highly variable genes: 1000-3000, number of neighbors: 15-30, n_pcs: 10-50, spread of UMAP: 1). Doublets assigned in subcluster analysis were removed, and the final embedding was generated following the same procedures. For marker gene detections, sc.tl.rank_genes_groups(method='wilcoxon') were used.

Cell deconvolution of Visium samples using Cell2location

Cell deconvolution of the Visium samples using Cell2location [12] was performed according to the tutorial guidelines (https://cell2location.readthedocs.io/en/latest/notebooks/cell2location_tutorial.html). The combined scRNA-seq reference without doublets (described below) was filtered (cell2location.util.filtering.filter_genes with the options cell_count_cutoff=5, cell_percentage_cutoff2=0.03, nonz_mean_cutoff=1.12) and prepared (cell2location.models.RegressionModel.setup_anndata with the options batch_key='sample', labels_key='clusterL2'). A regression model was created using cell2location.models.RegressionModel and trained (model training with max_epochs=250). Cell proportions were inferred for each Visium sample at each time point. In the inference step, a model for the Visium sample was created using cell2location.models.Cell2location(N_cells_per_location=30, detection_alpha=20) and trained (max_epochs=30000). Co-localization analysis was performed using cell2location.run_colocation(model_name='CoLocatedGroupsSklearnNMF'), and the optimal number of factors was manually selected.

Cell deconvolution of TCGA bulk RNA-seq samples using Scaden

Cell deconvolution of TCGA samples was performed using a neural-net-based algorithm, Scaden (v1.1.1), as described by Yasumizu *et al.* [6]. We created 30,000 simulation datasets using a scaden simulate. The count matrices of our single-cell dataset and the TCGA thymoma dataset quantified by HTseq and downloaded from TCGAbilkinks were pre-processed using the scaden process command. Thereafter, the network was trained using the command, scaden train with the option, --steps 5000. Finally, the bulk RNA-seq matrix was deconvoluted using scaden predict. The deconvoluted cell proportion was tested using a multiple linear regression provided as the formula.api.ols function using the Python package statsmodels (0.12.0) with a model, cells ~ MG + WHO + days_to_birth + Gender + 1.

Cell-cell interaction analysis by CellphoneDB

CCI inference was performed using the CellphoneDB [19] framework. Cells with a loading of 0.1 or higher in the NMF-based cell co-localization analysis of Cell2location were used as the microenvironments. CCI inference was performed using the cellphonedb.src.core.methods.cpdb_statistical_analysis_method.call (score_interactions=True, threshold=0.1) function. The results were visualized using ktplotspy and Scanpy software.

Data and material availability

Datasets and codes will be available upon publication.

Acknowledgments

This work was supported by the Grants-in-Aid for Scientific Research Grant 23H02826 from the Ministry of Education, Culture, Sports, Science, and Technology of Japan. Y. Y. was supported by the Takeda Science Foundation. We acknowledge the NGS core facility of the Genome Information Research Center at the Research Institute for Microbial Diseases of Osaka University for its support in Sequencing as well as the BIKEN Foundation for preparing tissue sections for visual analysis. This work was partly achieved through the use of SQUID at the Cybermedia Center, Osaka University. The illustrations were generated using BioRender.com.

Author contributions

Y.Y., M.K., and T.O. designed all experiments; Y.Y. performed the bioinformatics analysis, prepared the figures, and drafted the manuscript; T.O. and Z.M. reviewed and edited the manuscript; D.M., K.S., and D.O. performed the experiments; S.N., S.F., Y.S., and E.M. provided samples for analysis; M.Z., S.N., and E.M. provided expert advice; and all authors critically reviewed and edited the final version of the manuscript.

Declaration of interests

The authors declare no competing interests.

Declaration of generative AI and AI-assisted technologies in the writing process

During the preparation of this study, the authors used ChatGPT4 to improve language and readability. After using this service, the authors reviewed and edited the content as needed and take full responsibility for the content of the publication.

Figure legends

Figure 1 Spatial transcriptomic analysis revealed histological structures in myasthenia gravis (MG) thymoma.

(A) Schematic representation of the spatial transcriptomic analysis and enrolled sample numbers. (B) Unsupervised clusters (Leiden) and annotation (Annotated Niche) of spots on UMAP plots. (C) Heatmap showing mean expression of marker genes in Annotated Niche groups. Also see Figure S1A for automatically-extracted marker genes. (D) Representative spatial gene expression of normal thymus and thymoma samples. (E) Distribution of disease status on UMAP plots. (F) Comparison of the proportion of annotated niches in thymoma samples. Statistical analysis was performed using scCODA [44]. (G) Hematoxylin and eosin (H&E) staining, Leiden clusters, and annotated niche groups of representative samples. The arrowheads indicate a lymphoid follicle. The scale bars indicate 100 µm.

Figure 2 single-cell disease-relevance score (scDRS)-spatial unveiled polygenic enrichment in the medulla in MG thymoma.

(A and B) Heatmaps show disease association in Leiden clusters (A) and annotated niche (B). Samples were stratified with disease conditions. Heatmap colors depict the proportion of significant cells (False Discovery Rate (FDR) < 0.2) evaluated using scDRS [13]. Squares denote significant disease associations (FDR < 0.05), and cross symbols denote significant heterogeneity in association (FDR < 0.05). (C) scDRS scores on representative Visium slides.

Figure 3 Cell deconvolution analysis revealed cellular composition in MG thymoma.

(A) Schematic of single-cell RNA-seq (scRNA-seq) reference construction and cell deconvolution analysis. (B) Cell clusters of the reference scRNAseq data on UMAP plot. (C) Cellular decomposition in each annotated niche group. Deconvolution was performed using Cell2location [12]. (D) Normalized cellular decomposition and H&E staining of representative Visium slides. The scale bars indicate 100 µm. (E) Normalized cellular decomposition in each disease condition. (F) Cell compartments identified using non-negative matrix factorization (NMF). The normalized NMF weights of cell types across NMF components are shown. (G and H) Distributions of cell compartments across Leiden clusters (G) and annotated niche groups (H). The abundance was normalized for each column.

Figure 4 Niche-specific cytokine organization identified by cell-cell interaction analysis.

(A) Dot plot showing cytokine expressions across annotated niche groups in the normal thymus (top) and thymoma (middle), and across major cell types (bottom). Gene expressions for annotated niche groups were from the Visium dataset, and those for the cell types were from scRNAseq. (B) Representative cytokine expression of a thymoma sample. Ligands (left) and receptors (right) are shown correspondingly per line.

Figure 5 Spatial characteristics of thymic hyperplasia

(A) H&E staining and annotated niche groups of a thymic hyperplasia sample. The arrowhead indicates a lymphoid follicle. The scale bar indicates 100 μm. (B) scDRS scores of representative Visium slides. (C) Heatmap shows disease association in annotated niches stratified by disease conditions. Heatmap colors depict the proportion of significant cells (FDR < 0.2) evaluated using scDRS [13]. Squares denote significant disease associations (FDR < 0.05), and cross symbols denote significant heterogeneity in association (FDR < 0.05). (D) Distributions of cell compartments defined by NMF. (E) Dot plot showing cytokine expressions across annotated niche groups in thymic hyperplasia. (F) Representative cytokine expression of a thymoma sample. Ligands (left) and receptors (right) are shown correspondingly per line.

Figure 6 Spatial features of MG thymoma.

Figure S1 Spatial characteristics of thymoma samples

(A) Dot plot showing marker gene expression for Leiden clusters. Three genes with Bayes_factor > 2 and non_zeros_proportion > 0.1 are shown for each cluster. Also see Table S2 for detailed statistics. (B) Distribution of disease status (top) and data sources (bottom) of UMAP plots. (C) Marker gene expression of UMAP plots. (D and E) Heatmap showing Pearson's correlation of mean expression across Leiden clusters (D) and annotated niche groups (E). (F) Heatmap showing spatial neighborhood enrichment of annotated niche groups. The calculation was performed using Squidpy [43]. (G) Comparison of the proportion of Leiden groups in thymoma samples. Statistical analysis was performed using scCODA [44]. (H and I) Dot plots showing changes in yellow module expression (MG signature genes) [6] across annotated niche groups (H) and Leiden groups (I) in thymoma. A generalized linear mixed model was applied (fixed effect: niche_annot or leiden, mixed effect: sample).

Figure S2 Annotated niche clusters of tissue sections.

Annotated niche clusters for all samples enrolled in this study.

Figure S3 scDRS-spatial framework to investigate the association between disease and spatial niche.

(A) Concept of scDRS-spatial. (B) Quantile-quantile plot of null simulations for scDRS [13] and scDRS with imputation by MAGIC [16]. Approximately 1,000 randomly selected genes were assessed using control tissue sections (Table S3). Error bars denote 95% confidence intervals around the mean of 100 simulation replicates. (C - E) Heatmaps show disease association in tissues (C), Leiden clusters (D), and annotated niches (E). Heatmap colors depict the proportion of significant cells (FDR < 0.2) evaluated using scDRS [13]. Squares denote significant disease associations (FDR < 0.05), and cross symbols denote significant heterogeneity in association (FDR < 0.05).

Figure S4 Single-cell atlas of thymoma.

(A) Overview of single-cell RNA-seq (scRNA-seq) atlas. Cluster layer 1 (L1) categories are shown on the UMAP plot (left), and the manually selected marker genes are shown in a dot plot. (B-F) Detailed features of cell types. Each subcluster was extracted, annotated (cluster L2), and re-embedded using UMAP (left). Marker genes are shown for each cluster as dot plots (right). (G) Dot plot showing the expression of migratory dendritic cell (migDC)-related genes of myeloid populations.

Figure S5 MG thymoma-specific features assessed using TCGA bulk RNA-seq data.

(A) Volcano plot showing the association between MG and deconvoluted cell proportions, which were calculated using The Cancer Genome Atlas (TCGA) [18] bulk RNA-seq dataset (n = 116) with the reference defined in our scRNAseq analysis. Coefficients and p-values were calculated with multiple regression (Methods). Red dots represent FDR < 0.05, and orange dots represent FDR < 0.2. (B) Enrichment analysis of gene modules using TCGA thymoma samples defined in Yasumizu *et al.* [6] using the scRNAseq reference. The yellow module is the MG-specific genes, as shown in the original article.

Figure S6 Additional information for Cell2location analysis.

(A) Normalized cellular decomposition in each annotated niche group. Deconvolution was performed using Cell2location [12]. (B) Associations of cell proportions with MG in thymoma samples. (C) Distributions of cell compartments defined by NMF. MG thymoma (upper panel) and non-MG thymoma (lower panel) are shown.

Figure S7 Additional information for cell-cell interaction analysis.

(A) Heatmap showing a number of significant interactions assessed by CellPhoneDB [19]. (B) Interactome of cytokines among immune cells.

Figure S8 Representative cytokine expressions.

(A and B) Representative cytokine expression of a non-MG thymoma sample (A) and a normal thymus sample (B). Ligands (left) and receptors (right) are shown correspondingly per line.

Figure S9 Additional information for scDRS-spatial analysis for thymic hyperplasia.

(A) Violin plot showing scDRS score in annotated niche groups in thymic hyperplasia samples. (B) Heatmaps show disease association in Leiden clusters stratified by disease conditions. Heatmap colors depict the proportion of significant cells ($FDR < 0.2$) evaluated using scDRS [13]. Squares denote significant disease associations (FDR□<□0.05), and cross symbols denote significant heterogeneity in association (FDR□<□0.05).

References

1. Chia, R., Saez-Atienzar, S., Murphy, N., Chiò, A., Blauwendraat, C., International Myasthenia Gravis Genomics Consortium, Roda, R.H., Tienari, P.J., Kaminski, H.J., Ricciardi, R., et al. (2022). Identification of genetic risk loci and prioritization of genes and pathways for myasthenia gravis: a genome-wide association study. Proc. Natl. Acad. Sci. U. S. A. *119*. 10.1073/pnas.2108672119.

2. Yasumizu, Y., Takeuchi, D., Morimoto, R., Takeshima, Y., Okuno, T., Kinoshita, M., Morita, T., Kato, Y., Wang, M., Motooka, D., et al. (2024). Single-cell transcriptome landscape of circulating CD4+ T cell populations in autoimmune diseases. Cell Genomics *0*. 10.1016/j.xgen.2023.100473.

3. Wolfe, G.I., Kaminski, H.J., Aban, I.B., Minisman, G., Kuo, H.-C., Marx, A., Ströbel, P., Mazia, C., Oger, J., Cea, J.G., et al. (2016). Randomized Trial of Thymectomy in Myasthenia Gravis. N. Engl. J. Med. *375*, 511–522.

4. Masaoka, A., Yamakawa, Y., Niwa, H., Fukai, I., Kondo, S., Kobayashi, M., Fujii, Y., and Monden, Y. (1996). Extended thymectomy for myasthenia gravis patients: a 20-year review. Ann. Thorac. Surg. *62*, 853–859.

5. Kooshesh, K.A., Foy, B.H., Sykes, D.B., Gustafsson, K., and Scadden, D.T. (2023). Health Consequences of Thymus Removal in Adults. N. Engl. J. Med. *389*, 406–417.

6. Yasumizu, Y., Ohkura, N., Murata, H., Kinoshita, M., Funaki, S., Nojima, S., Kido, K., Kohara, M., Motooka, D., Okuzaki, D., et al. (2022). Myasthenia gravis-specific aberrant neuromuscular gene expression by medullary thymic epithelial cells in thymoma. Nat. Commun. *13*, 4230.

7. Cron, M.A., Maillard, S., Villegas, J., Truffault, F., Sudres, M., Dragin, N., Berrih-Aknin, S., and Le Panse, R. (2018). Thymus involvement in early-onset myasthenia gravis. Ann. N. Y. Acad. Sci. *1412*, 137–145.

8. Levine, G.D., and Rosai, J. (1978). Thymic hyperplasia and neoplasia: a review of current concepts. Hum. Pathol. *9*, 495–515.

9. Kanemaru, K., Cranley, J., Muraro, D., Miranda, A.M.A., Ho, S.Y., Wilbrey-Clark, A., Patrick Pett, J., Polanski, K., Richardson, L., Litvinukova, M., et al. (2023). Spatially resolved multiomics of

human cardiac niches. Nature *619*, 801–810.

10. Lerma-Martin, C., Badia-i-Mompel, P., Ramirez Flores, R.O., Sekol, P., Hofmann, A., Thäwel, T., Riedl, C.J., Wünnemann, F., Ibarra-Arellano, M.A., Trobisch, T., et al. (2022). Spatial cell type mapping of multiple sclerosis lesions. bioRxiv, 2022.11.03.514906. 10.1101/2022.11.03.514906.

11. Rao, A., Barkley, D., França, G.S., and Yanai, I. (2021). Exploring tissue architecture using spatial transcriptomics. Nature *596*, 211–220.

12. Kleshchevnikov, V., Shmatko, A., Dann, E., Aivazidis, A., King, H.W., Li, T., Elmentaite, R., Lomakin, A., Kedlian, V., Gayoso, A., et al. (2022). Cell2location maps fine-grained cell types in spatial transcriptomics. Nat. Biotechnol. *40*, 661–671.

13. Zhang, M.J., Hou, K., Dey, K.K., Sakaue, S., Jagadeesh, K.A., Weinand, K., Taychameekiatchai, A., Rao, P., Pisco, A.O., Zou, J., et al. (2022). Polygenic enrichment distinguishes disease associations of individual cells in single-cell RNA-seq data. Nat. Genet., 1–9.

14. Xin, Z., Lin, M., Hao, Z., Chen, D., Chen, Y., Chen, X., Xu, X., Li, J., Wu, D., Chai, Y., et al. (2022). The immune landscape of human thymic epithelial tumors. Nat. Commun. *13*, 5463.

15. Marx, A., Ströbel, P., and Weis, C.-A. (2018). The pathology of the thymus in myasthenia gravis. Mediastinum *2*, 66–66.

16. van Dijk, D., Sharma, R., Nainys, J., Yim, K., Kathail, P., Carr, A.J., Burdziak, C., Moon, K.R., Chaffer, C.L., Pattabiraman, D., et al. (2018). Recovering Gene Interactions from Single-Cell Data Using Data Diffusion. Cell *174*, 716–729.e27.

17. Sugiura, D., Maruhashi, T., Okazaki, I.-M., Shimizu, K., Maeda, T.K., Takemoto, T., and Okazaki, T. (2019). Restriction of PD-1 function by *cis*-PD-L1/CD80 interactions is required for optimal T cell responses. Science *364*, 558–566.

18. Hoadley, K.A., Yau, C., Hinoue, T., Wolf, D.M., Lazar, A.J., Drill, E., Shen, R., Taylor, A.M., Cherniack, A.D., Thorsson, V., et al. (2018). Cell-of-Origin Patterns Dominate the Molecular Classification of 10,000 Tumors from 33 Types of Cancer. Cell *173*, 291–304.e6.

19. Garcia-Alonso, L., Handfield, L.-F., Roberts, K., Nikolakopoulou, K., Fernando, R.C., Gardner, L., Woodhams, B., Arutyunyan, A., Polanski, K., Hoo, R., et al. (2021). Mapping the temporal and spatial dynamics of the human endometrium in vivo and in vitro. Nat. Genet. *53*, 1698–1711.

20. Nakandakari-Higa, S., Canesso, M.C.C., Walker, S., Chudnovskiy, A., Jacobsen, J.T., Bilanovic, J., Parigi, S.M., Fiedorczuk, K., Fuchs, E., Bilate, A.M., et al. (2023). Universal recording of cell-cell contacts in vivo for interaction-based transcriptomics. bioRxiv. 10.1101/2023.03.16.533003.

21. Yamada, Y. (2023). Histogenetic and disease-relevant phenotypes in thymic epithelial tumors (TETs): The potential significance for future TET classification. Pathol. Int. *73*, 265–280.

22. Marx, A., Yamada, Y., Simon-Keller, K., Schalke, B., Willcox, N., Ströbel, P., and Weis, C.-A. (2021). Thymus and autoimmunity. Semin. Immunopathol. *43*, 45–64.

23. Park, J.-E., Botting, R.A., Domínguez Conde, C., Popescu, D.-M., Lavaert, M., Kunz, D.J., Goh, I., Stephenson, E., Ragazzini, R., Tuck, E., et al. (2020). A cell atlas of human thymic development defines T cell repertoire formation. Science *367*, 2020.01.28.911115.

24. Kadouri, N., Nevo, S., Goldfarb, Y., and Abramson, J. (2020). Thymic epithelial cell heterogeneity: TEC by TEC. Nat. Rev. Immunol. *20*, 239–253.

25. Anderson, M.S., Venanzi, E.S., Klein, L., Chen, Z., Berzins, S.P., Turley, S.J., von Boehmer, H., Bronson, R., Dierich, A., Benoist, C., et al. (2002). Projection of an immunological self shadow within the thymus by the aire protein. Science *298*, 1395–1401.

26. Aschenbrenner, K., D'Cruz, L.M., Vollmann, E.H., Hinterberger, M., Emmerich, J., Swee, L.K., Rolink, A., and Klein, L. (2007). Selection of Foxp3+ regulatory T cells specific for self antigen expressed and presented by Aire+ medullary thymic epithelial cells. Nat. Immunol. *8*, 351–358.

27. Li, J., Zhou, J., Huang, H., Jiang, J., Zhang, T., and Ni, C. (2023). Mature dendritic cells enriched in immunoregulatory molecules (mregDCs): A novel population in the tumour microenvironment and immunotherapy target. Clin. Transl. Med. *13*, e1199.

28. Magen, A., Hamon, P., Fiaschi, N., Soong, B.Y., Park, M.D., Mattiuz, R., Humblin, E., Troncoso, L., D'souza, D., Dawson, T., et al. (2023). Intratumoral dendritic cell-CD4+ T helper cell niches enable CD8+ T cell differentiation following PD-1 blockade in hepatocellular carcinoma. Nat. Med. *29*, 1389–1399.

29. Zuckerman, N.S., Howard, W.A., Bismuth, J., Gibson, K., Edelman, H., Berrih-Aknin, S., Dunn-Walters, D., and Mehr, R. (2010). Ectopic GC in the thymus of myasthenia gravis patients show characteristics of normal GC. Eur. J. Immunol. *40*, 1150–1161.

30. Sims, G.P., Shiono, H., Willcox, N., and Stott, D.I. (2001). Somatic hypermutation and selection of B cells in thymic germinal centers responding to acetylcholine receptor in myasthenia gravis. J. Immunol. *167*, 1935–1944.

31. Bocharnikov, A.V., Keegan, J., Wacleche, V.S., Cao, Y., Fonseka, C.Y., Wang, G., Muise, E.S., Zhang, K.X., Arazi, A., Keras, G., et al. (2019). PD-1hiCXCR5- T peripheral helper cells promote B cell responses in lupus via MAF and IL-21. JCI Insight *4*. 10.1172/jci.insight.130062.

32. Pontarini, E., Murray-Brown, W.J., Croia, C., Lucchesi, D., Conway, J., Rivellese, F., Fossati-Jimack, L., Astorri, E., Prediletto, E., Corsiero, E., et al. (2020). Unique expansion of IL-21+ Tfh and Tph cells under control of ICOS identifies Sjögren's syndrome with ectopic germinal centres and MALT lymphoma. Ann. Rheum. Dis. *79*, 1588–1599.

33. Rao, D.A., Gurish, M.F., Marshall, J.L., Slowikowski, K., Fonseka, C.Y., Liu, Y., Donlin, L.T., Henderson, L.A., Wei, K., Mizoguchi, F., et al. (2017). Pathologically expanded peripheral T helper cell subset drives B cells in rheumatoid arthritis. Nature *542*, 110–114.

34. Çebi, M., Durmus, H., Aysal, F., Özkan, B., Gül, G.E., Çakar, A., Hocaoglu, M., Mercan, M., Yentür, S.P., Tütüncü, M., et al. (2020). CD4+ T Cells of Myasthenia Gravis Patients Are Characterized by Increased IL-21, IL-4, and IL-17A Productions and Higher Presence of PD-1 and ICOS. Front. Immunol. *11*, 809.

35. Gradolatto, A., Nazzal, D., Truffault, F., Bismuth, J., Fadel, E., Foti, M., and Berrih-Aknin, S. (2014). Both Treg cells and Tconv cells are defective in the Myasthenia gravis thymus: roles of IL-17 and TNF-α. J. Autoimmun. *52*, 53–63.

36. Yamamoto, Y., Matsui, N., Uzawa, A., Ozawa, Y., Kanai, T., Oda, F., Kondo, H., Ohigashi, I., Takizawa, H., Kondo, K., et al. (2021). Intrathymic Plasmablasts Are Affected in Patients With Myasthenia Gravis With Active Disease. Neurol Neuroimmunol Neuroinflamm *8*. 10.1212/NXI.0000000000001087.

37. Jiang, R., Hoehn, K.B., Lee, C.S., Pham, M.C., Homer, R.J., Detterbeck, F.C., Aban, I., Jacobson, L., Vincent, A., Nowak, R.J., et al. (2020). Thymus-derived B cell clones persist in the circulation after thymectomy in myasthenia gravis. Proc. Natl. Acad. Sci. U. S. A. *117*, 30649–30660.

38. Fujii, Y., Monden, Y., Hashimoto, J., Nakahara, K., and Kawashima, Y. (1985). Acetylcholine receptor antibody production by bone marrow cells in a patient with myasthenia gravis. Neurology *35*, 577–579.

39. Heimli, M., Flåm, S.T., Hjorthaug, H.S., Trinh, D., Frisk, M., Dumont, K.-A., Ribarska, T., Tekpli, X., Saare, M., and Lie, B.A. (2022). Multimodal human thymic profiling reveals trajectories and cellular milieu for T agonist selection. Front. Immunol. *13*, 1092028.

40. Suo, C., Dann, E., Goh, I., Jardine, L., Kleshchevnikov, V., Park, J.-E., Botting, R.A., Stephenson, E., Engelbert, J., Tuong, Z.K., et al. (2022). Mapping the developing human immune system across organs. Science *376*, eabo0510.

41. Wolf, F.A., Angerer, P., and Theis, F.J. (2018). SCANPY: large-scale single-cell gene expression data analysis. Genome Biol. *19*, 15.

42. Lopez, R., Regier, J., Cole, M., Jordan, M., and Yosef, N. (2018). Bayesian Inference for a Generative Model of Transcriptome Profiles from Single-cell RNA Sequencing. 10.1101/292037.

43. Palla, G., Spitzer, H., Klein, M., Fischer, D., Schaar, A.C., Kuemmerle, L.B., Rybakov, S., Ibarra, I.L., Holmberg, O., Virshup, I., et al. (2022). Squidpy: a scalable framework for spatial omics analysis. Nat. Methods *19*, 171–178.

44. Büttner, M., Ostner, J., Müller, C.L., Theis, F.J., and Schubert, B. (2021). scCODA is a Bayesian model for compositional single-cell data analysis. Nat. Commun. *12*, 6876.

45. de Leeuw, C.A., Mooij, J.M., Heskes, T., and Posthuma, D. (2015). MAGMA: generalized gene-set analysis of GWAS data. PLoS Comput. Biol. *11*, e1004219.

46. Wolock, S.L., Lopez, R., and Klein, A.M. (2019). Scrublet: Computational Identification of Cell Doublets in Single-Cell Transcriptomic Data. Cell Systems *8*, 281–291.e9.

47. Korsunsky, I., Millard, N., Fan, J., Slowikowski, K., Zhang, F., Wei, K., Baglaenko, Y., Brenner, M., Loh, P. ru, and Raychaudhuri, S. (2019). Fast, sensitive and accurate integration of single-cell data with Harmony. Nat. Methods *16*, 1289–1296.

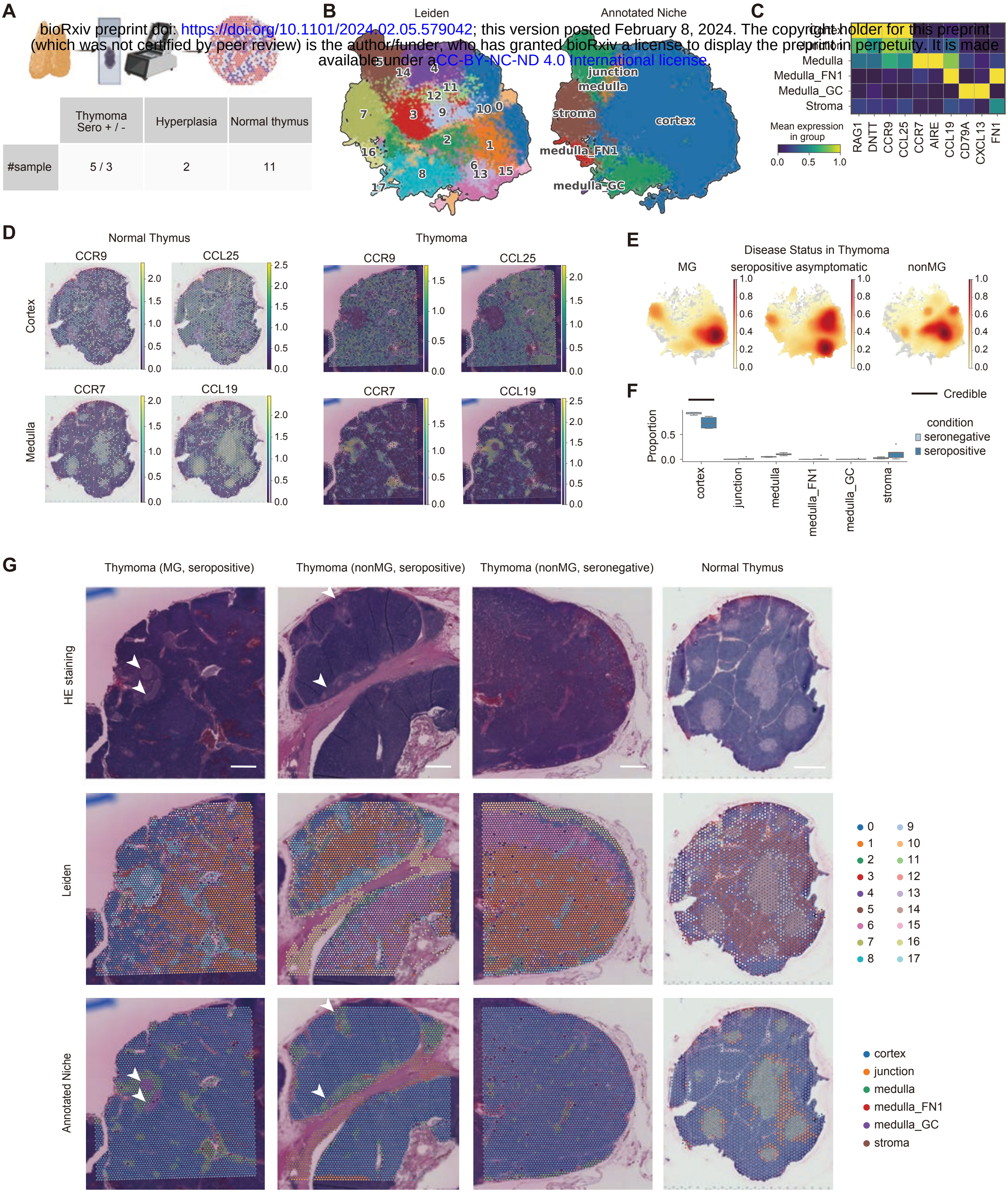
A
Thymoma Sero + / -
Hyperplasia
Normal thymus
#sample
5 / 3
2
11
B
Leiden
Annotated Niche
junction
medulla
stroma
cortex
medulla_FN1
medulla_GC
C
Cortex
Junction
Medulla
Medulla_FN1
Medulla_GC
Stroma
Mean expression in group
0.0
0.5
1.0
RAG1
DNTT
CCR9
CCL25
CCR7
AIRE
CCL19
CD79A
CXCL13
FN1
D
Normal Thymus
Thymoma
Cortex
Medulla
CCR9
CCL25
CCR7
CCL19
E
Disease Status in Thymoma
MG
seropositive asymptomatic
nonMG
F
Credible
Proportion
condition
seronegative
seropositive
cortex
junction
medulla
medulla_FN1
medulla_GC
stroma
G
Thymoma (MG, seropositive)
Thymoma (nonMG, seropositive)
Thymoma (nonMG, seronegative)
Normal Thymus
HE staining
Leiden
Annotated Niche
cortex
junction
medulla
medulla_FN1
medulla_GC
stroma

Figure 1

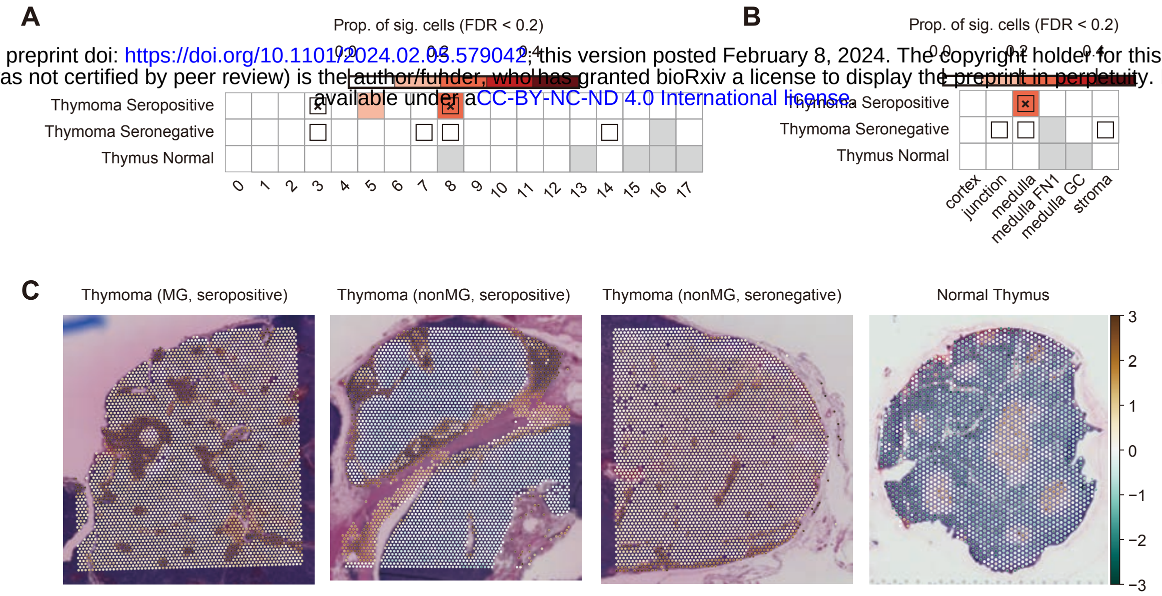
A
Prop. of sig. cells (FDR < 0.2)
0.0
0.2
0.4
Thymoma Seropositive
Thymoma Seronegative
Thymus Normal
0
1
2
3
4
5
6
7
8
9
10
11
12
13
14
15
16
17
B
Prop. of sig. cells (FDR < 0.2)
0.0
0.2
0.4
Thymoma Seropositive
Thymoma Seronegative
Thymus Normal
cortex
junction
medulla
medulla FN1
medulla GC
stroma
C
Thymoma (MG, seropositive)
Thymoma (nonMG, seropositive)
Thymoma (nonMG, seronegative)
Normal Thymus
3
2
1
0
−1
−2
−3

Figure 2

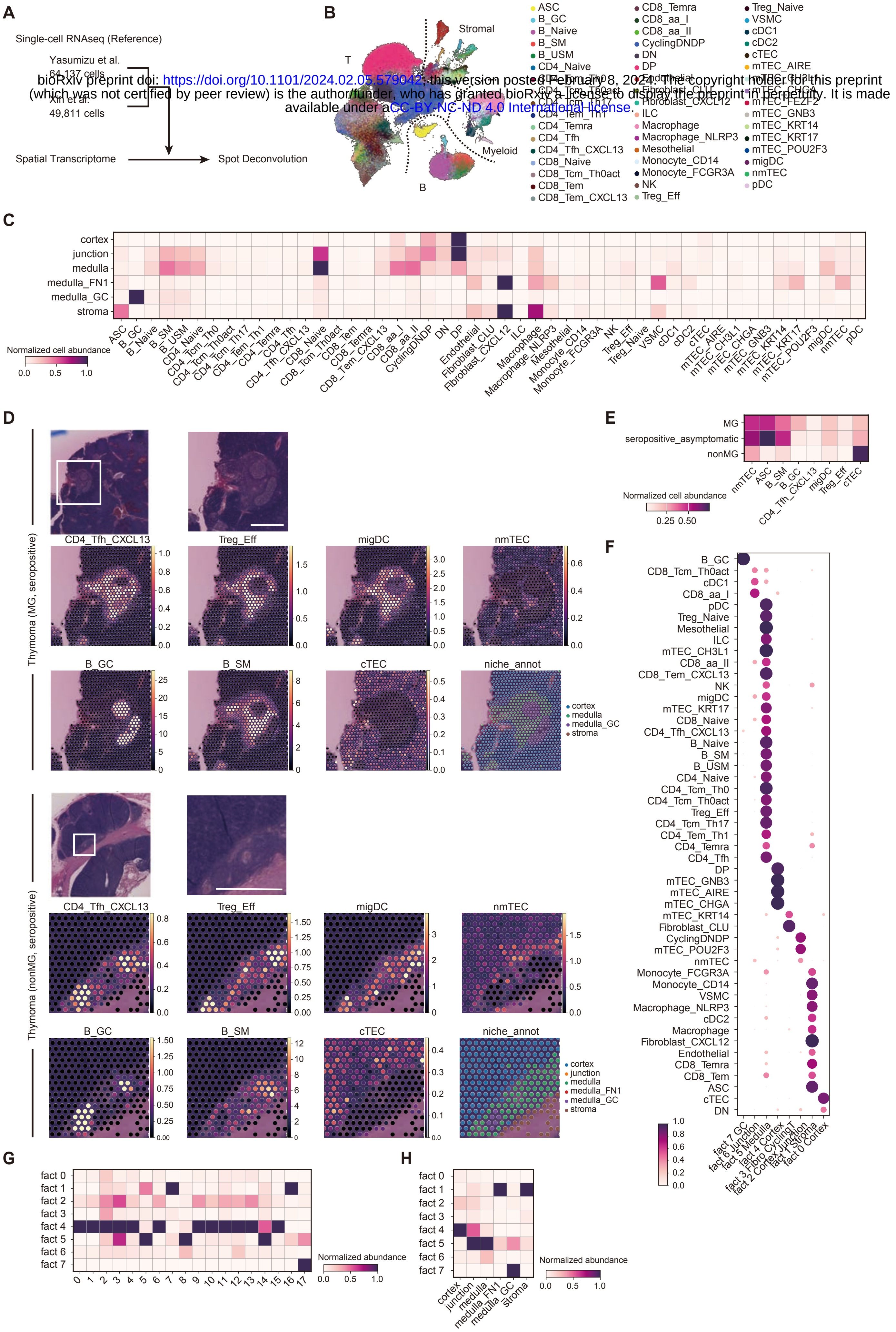
A
Single-cell RNAseq (Reference)
Yasumizu et al.
64,137 cells
Xin et al.
49,811 cells
Spatial Transcriptome
Spot Deconvolution
B
Stromal
T
Myeloid
B
ASC
B_GC
B_Naive
B_SM
B_USM
CD4_Naive
CD4_Tcm_Th0
CD4_Tcm_Th0act
CD4_Tcm_Th17
CD4_Tem_Th1
CD4_Temra
CD4_Tfh
CD4_Tfh_CXCL13
CD8_Naive
CD8_Tcm_Th0act
CD8_Tem
CD8_Tem_CXCL13
CD8_Temra
CD8_aa_I
CD8_aa_II
CyclingDNDP
DN
DP
Endothelial
Fibroblast_CLU
Fibroblast_CXCL12
ILC
Macrophage
Macrophage_NLRP3
Mesothelial
Monocyte_CD14
Monocyte_FCGR3A
NK
Treg_Eff
Treg_Naive
VSMC
cDC1
cDC2
cTEC
mTEC_AIRE
mTEC_CH3L1
mTEC_CHGA
mTEC_FEZF2
mTEC_GNB3
mTEC_KRT14
mTEC_KRT17
mTEC_POU2F3
migDC
nmTEC
pDC
C
cortex
junction
medulla
medulla_FN1
medulla_GC
stroma
Normalized cell abundance
0.0 0.5 1.0
D
Thymoma (MG, seropositive)
CD4_Tfh_CXCL13
Treg_Eff
migDC
nmTEC
B_GC
B_SM
cTEC
niche_annot
cortex
medulla
medulla_GC
stroma
Thymoma (nonMG, seropositive)
cortex
junction
medulla
medulla_FN1
medulla_GC
stroma
E
MG
seropositive_asymptomatic
nonMG
nmTEC
ASC
B_SM
B_GC
CD4_Tfh_CXCL13
migDC
Treg_Eff
cTEC
Normalized cell abundance
0.25 0.50
F
fact 7 GC
fact 6 Junction
fact 5 Medulla
fact 4 Cortex
fact 3 Fibro CyclingT
fact 2 Cortex Junction
fact 1 Stroma
fact 0 Cortex
1.0 0.8 0.6 0.4 0.2 0.0
G
fact 0
fact 1
fact 2
fact 3
fact 4
fact 5
fact 6
fact 7
0 1 2 3 4 5 6 7 8 9 10 11 12 13 14 15 16 17
Normalized abundance
0.0 0.5 1.0
H
cortex
junction
medulla
medulla_FN1
medulla_GC
stroma
Normalized abundance
0.0 0.5 1.0

Figure 3

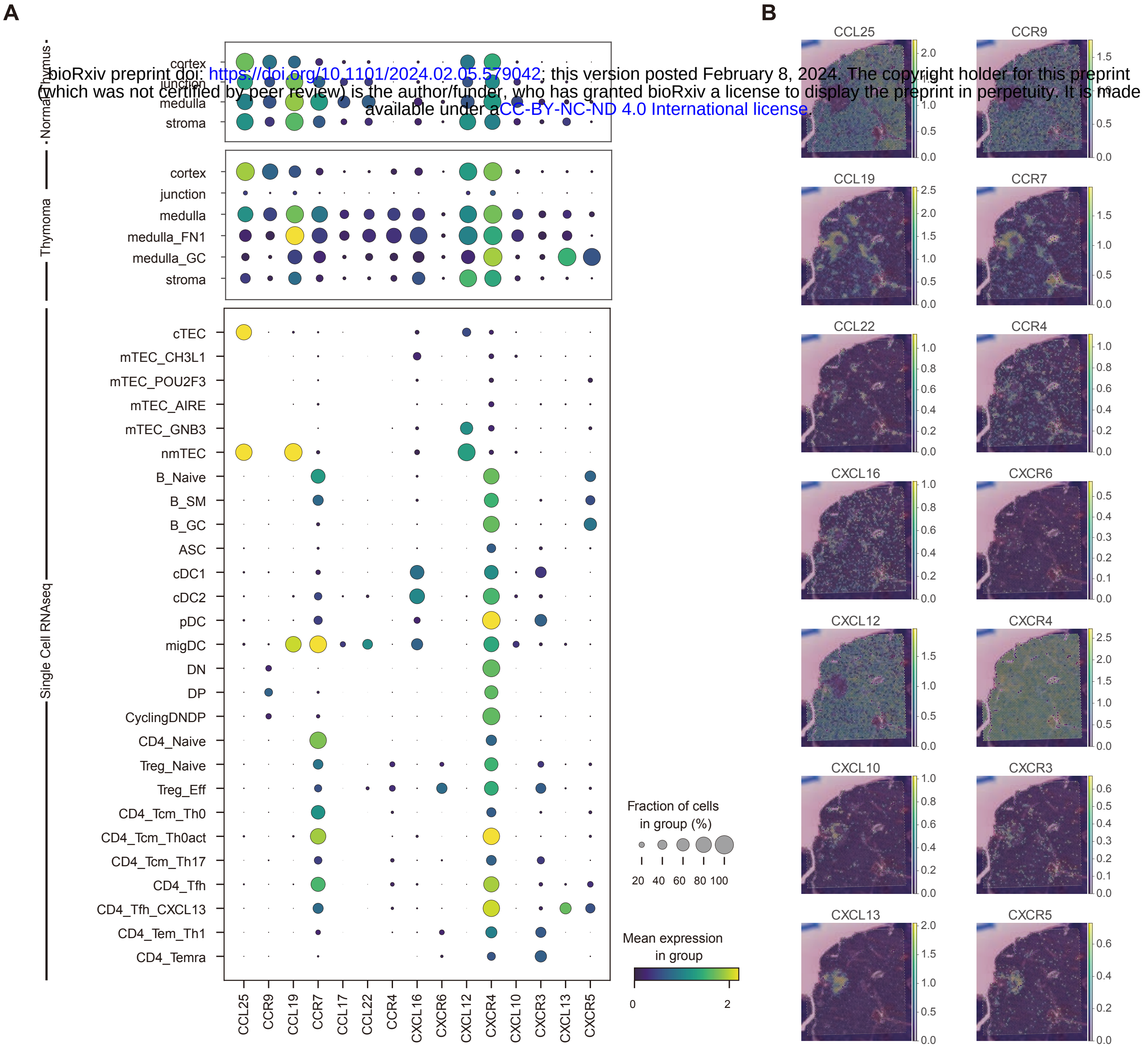
A
Normal Thymus
cortex
junction
medulla
stroma
Thymoma
cortex
junction
medulla
medulla_FN1
medulla_GC
stroma
Single Cell RNAseq
cTEC
mTEC_CH3L1
mTEC_POU2F3
mTEC_AIRE
mTEC_GNB3
nmTEC
B_Naive
B_SM
B_GC
ASC
cDC1
cDC2
pDC
migDC
DN
DP
CyclingDNDP
CD4_Naive
Treg_Naive
Treg_Eff
CD4_Tcm_Th0
CD4_Tcm_Th0act
CD4_Tcm_Th17
CD4_Tfh
CD4_Tfh_CXCL13
CD4_Tem_Th1
CD4_Temra
CCL25
CCR9
CCL19
CCR7
CCL17
CCL22
CCR4
CXCL16
CXCR6
CXCL12
CXCR4
CXCL10
CXCR3
CXCL13
CXCR5
Fraction of cells
in group (%)
20 40 60 80 100
Mean expression
in group
0
2
B
CCL25
CCR9
CCL19
CCR7
CCL22
CCR4
CXCL16
CXCR6
CXCL12
CXCR4
CXCL10
CXCR3
CXCL13
CXCR5

Figure 4

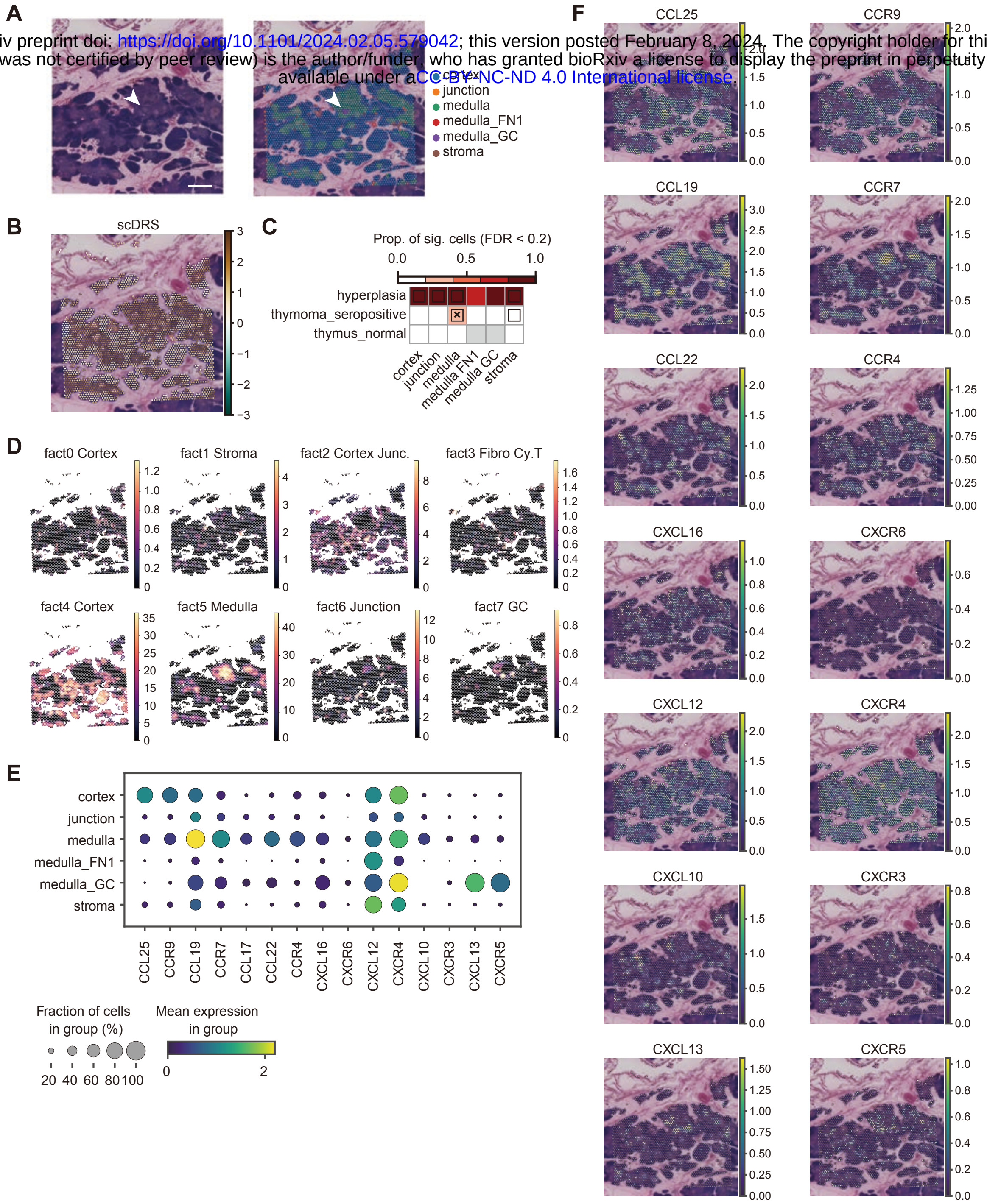
A
cortex
junction
medulla
medulla_FN1
medulla_GC
stroma
B
scDRS
C
Prop. of sig. cells (FDR < 0.2)
0.0
0.5
1.0
hyperplasia
thymoma_seropositive
thymus_normal
cortex
junction
medulla
medulla FN1
medulla GC
stroma
D
fact0 Cortex
fact1 Stroma
fact2 Cortex Junc.
fact3 Fibro Cy.T
fact4 Cortex
fact5 Medulla
fact6 Junction
fact7 GC
E
cortex
junction
medulla
medulla_FN1
medulla_GC
stroma
CCL25
CCR9
CCL19
CCR7
CCL17
CCL22
CCR4
CXCL16
CXCR6
CXCL12
CXCR4
CXCL10
CXCR3
CXCL13
CXCR5
Fraction of cells in group (%)
20 40 60 80 100
Mean expression in group
0
2
F
CCL25
CCR9
CCL19
CCR7
CCL22
CCR4
CXCL16
CXCR6
CXCL12
CXCR4
CXCL10
CXCR3
CXCL13
CXCR5

Figure 5

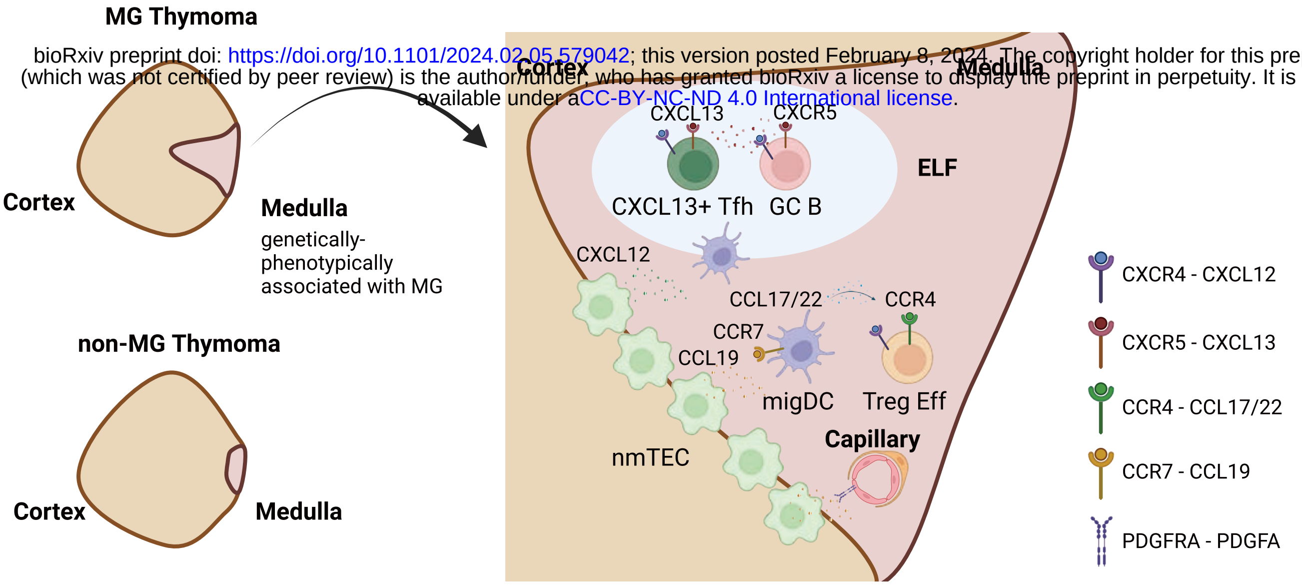
MG Thymoma
Cortex
Medulla
genetically-
phenotypically
associated with MG
non-MG Thymoma
Cortex
Medulla
Cortex
Medulla
CXCL13
CXCR5
ELF
CXCL13+ Tfh
GC B
CXCL12
CCL17/22
CCR4
CCR7
CCL19
migDC
Treg Eff
Capillary
nmTEC
CXCR4 - CXCL12
CXCR5 - CXCL13
CCR4 - CCL17/22
CCR7 - CCL19
PDGFRA - PDGFA

Figure 6

Figure S1

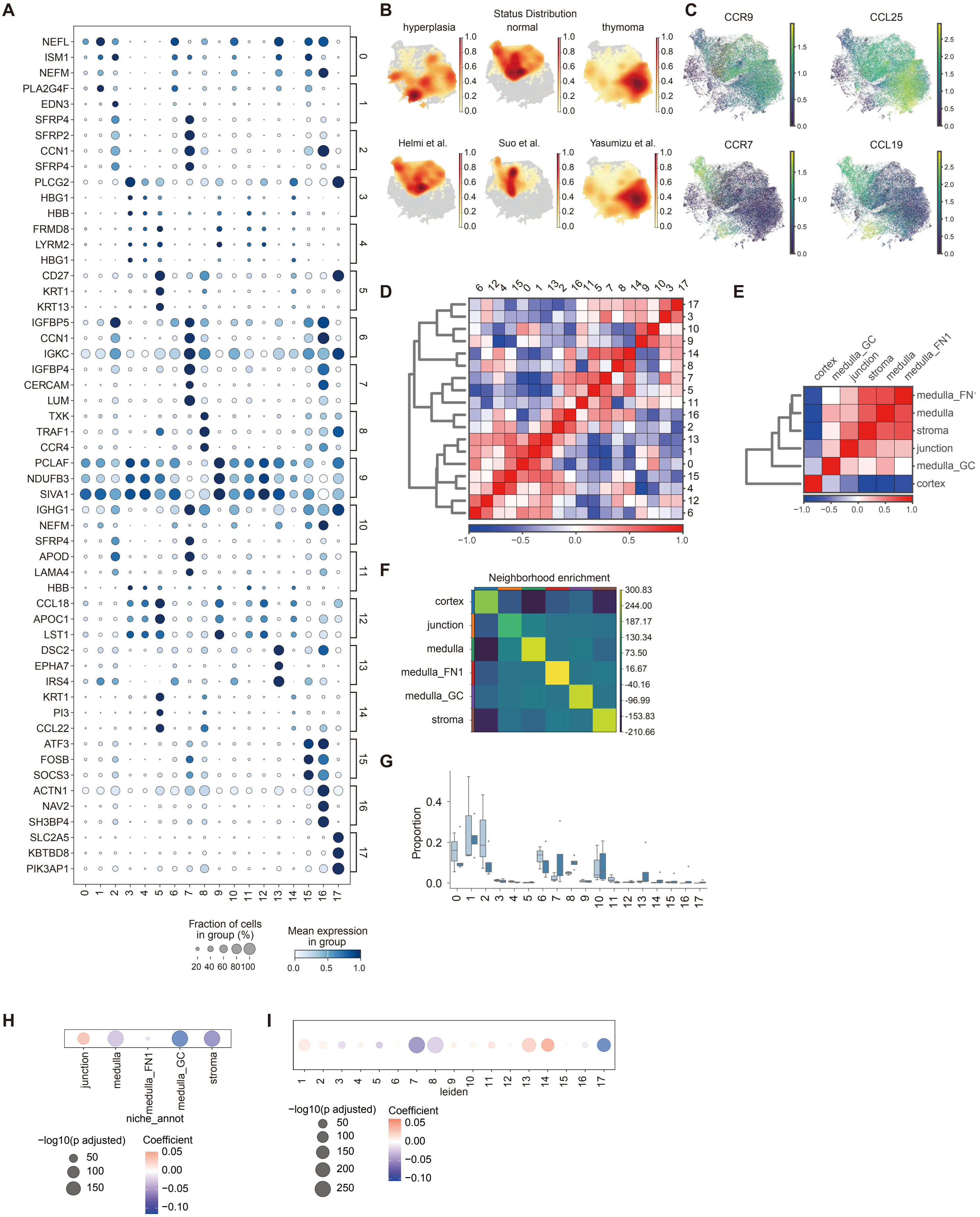
A
NEFL
ISM1
NEFM
PLA2G4F
EDN3
SFRP4
SFRP2
CCN1
SFRP4
PLCG2
HBG1
HBB
FRMD8
LYRM2
HBG1
CD27
KRT1
KRT13
IGFBP5
CCN1
IGKC
IGFBP4
CERCAM
LUM
TXK
TRAF1
CCR4
PCLAF
NDUFB3
SIVA1
IGHG1
NEFM
SFRP4
APOD
LAMA4
HBB
CCL18
APOC1
LST1
DSC2
EPHA7
IRS4
KRT1
PI3
CCL22
ATF3
FOSB
SOCS3
ACTN1
NAV2
SH3BP4
SLC2A5
KBTBD8
PIK3AP1
0 1 2 3 4 5 6 7 8 9 10 11 12 13 14 15 16 17
Fraction of cells in group (%)
20 40 60 80 100
Mean expression in group
0.0 0.5 1.0
B
Status Distribution
hyperplasia
normal
thymoma
Helmi et al.
Suo et al.
Yasumizu et al.
0.0 0.2 0.4 0.6 0.8 1.0
C
CCR9
CCL25
CCR7
CCL19
0.0 0.5 1.0 1.5 2.0 2.5
D
6 12 4 15 0 1 13 2 16 11 5 7 8 14 9 10 3 17
17 3 10 9 14 8 7 5 11 16 2 13 1 0 15 4 12 6
−1.0 −0.5 0.0 0.5 1.0
E
cortex medulla_GC junction stroma medulla medulla_FN1
medulla_FN1
medulla
stroma
junction
medulla_GC
cortex
−1.0 −0.5 0.0 0.5 1.0
F
Neighborhood enrichment
cortex
junction
medulla
medulla_FN1
medulla_GC
stroma
300.83
244.00
187.17
130.34
73.50
16.67
-40.16
-96.99
-153.83
-210.66
G
Proportion
0.0 0.2 0.4
0 1 2 3 4 5 6 7 8 9 10 11 12 13 14 15 16 17
H
junction
medulla
medulla_FN1
medulla_GC
stroma
niche_annot
−log10(p adjusted)
50
100
150
Coefficient
0.05
0.00
−0.05
−0.10
I
1 2 3 4 5 6 7 8 9 10 11 12 13 14 15 16 17
leiden
−log10(p adjusted)
50
100
150
200
250
Coefficient
0.05
0.00
−0.05
−0.10

Figure S2

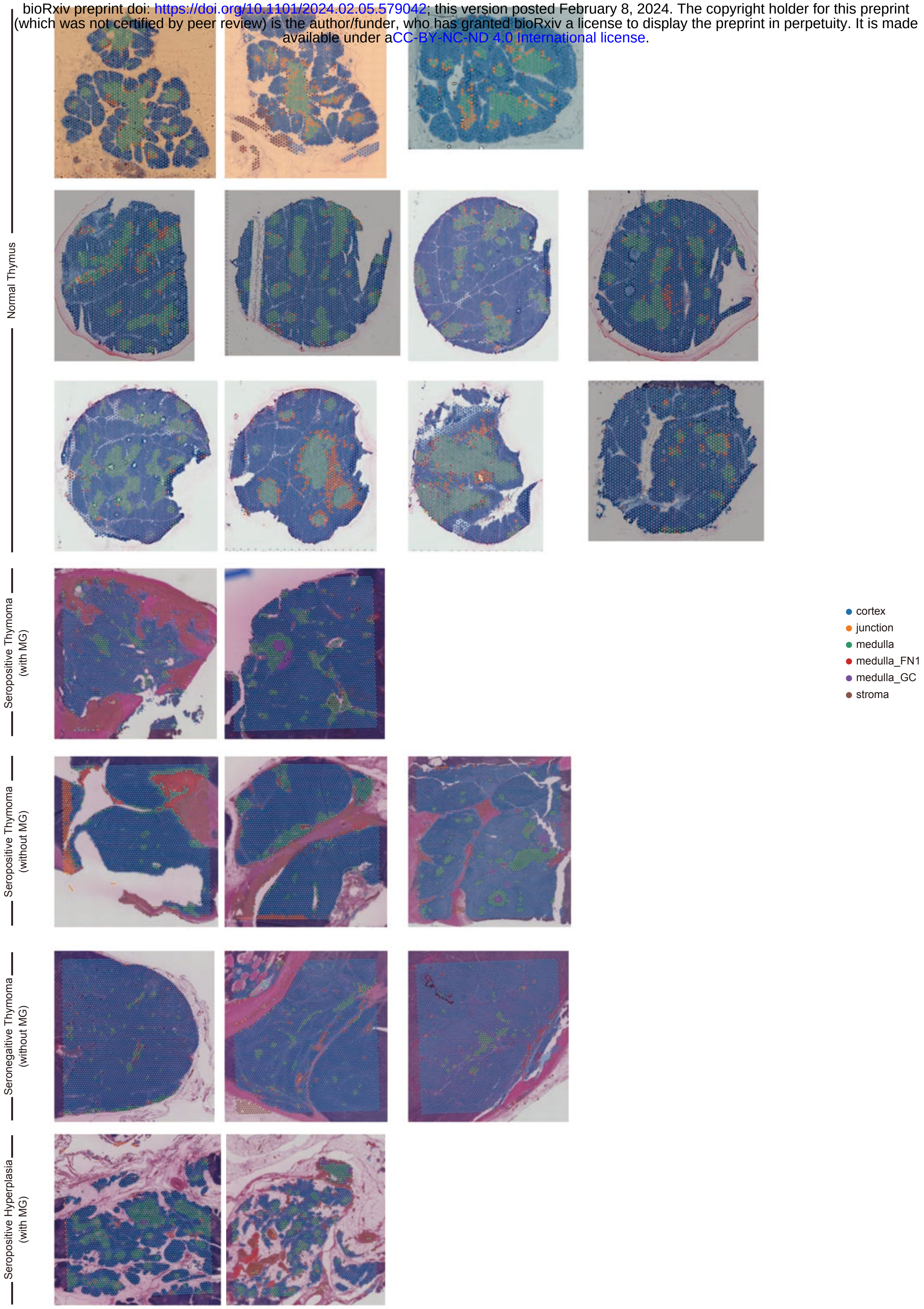
Normal Thymus
Seropositive Thymoma (with MG)
Seropositive Thymoma (without MG)
Seronegaitive Thymoma (without MG)
Seropositive Hyperplasia (with MG)
● cortex
● junction
● medulla
● medulla_FN1
● medulla_GC
● stroma

Figure S3

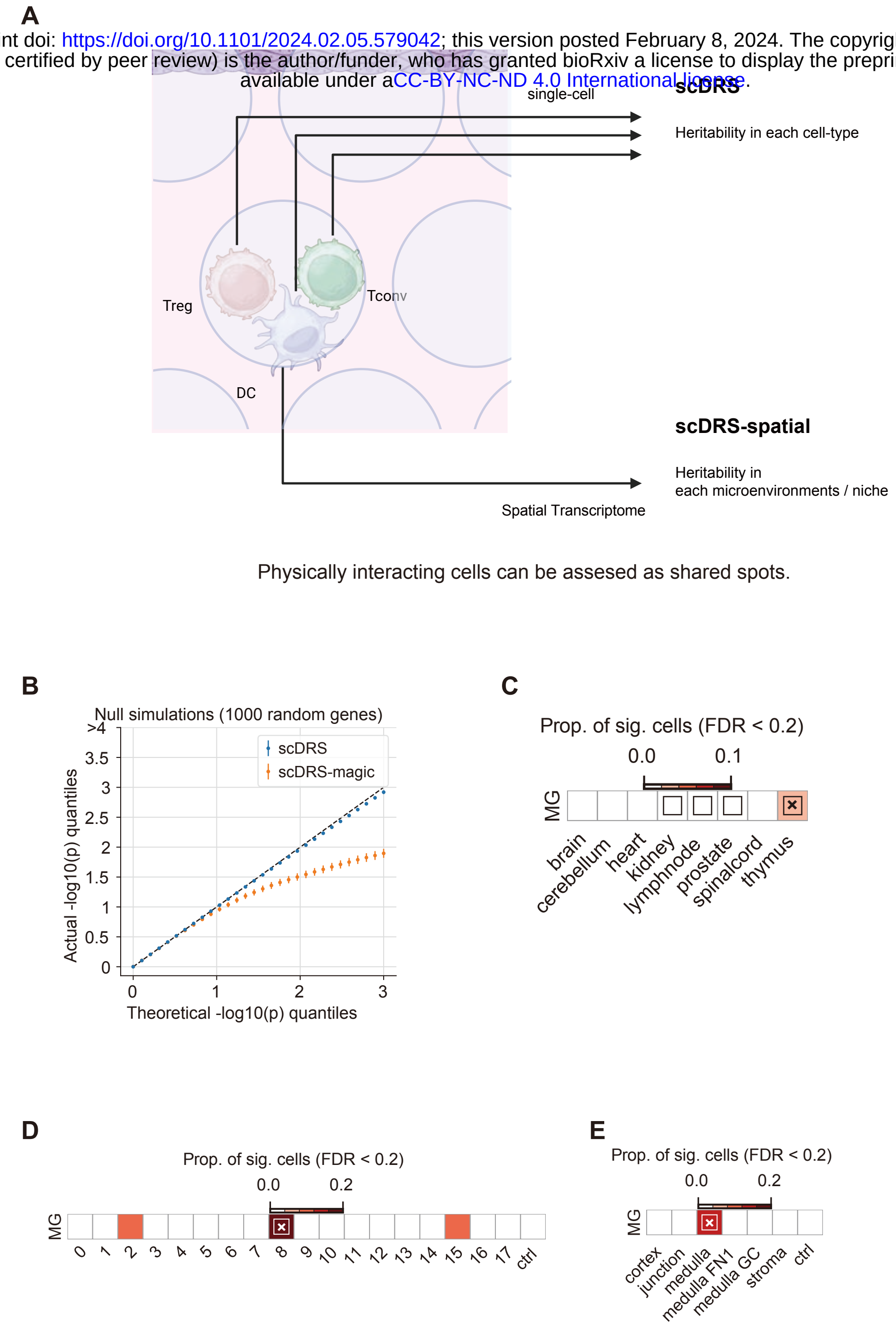

Physically interacting cells can be assesed as shared spots.

Figure S4

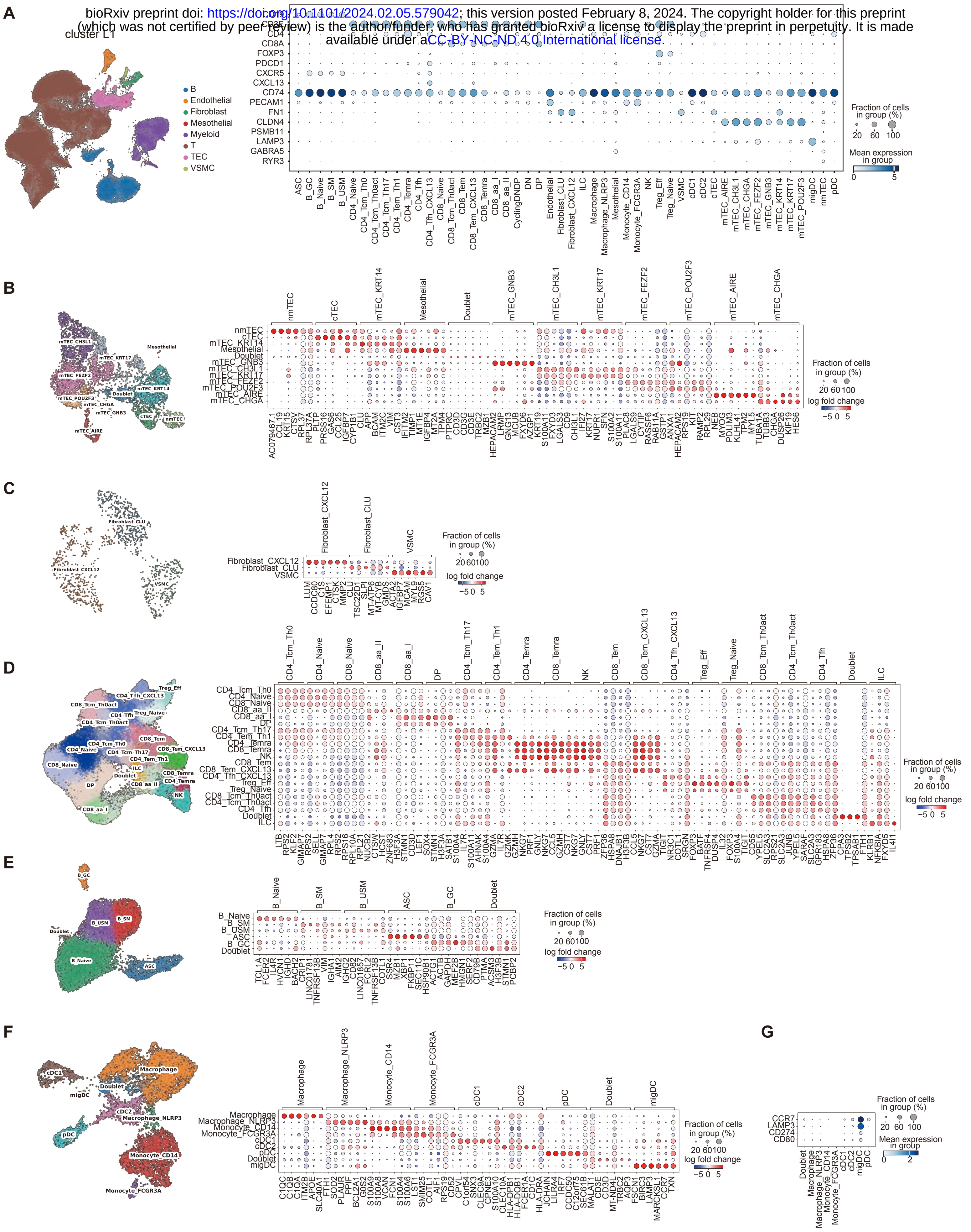
A
cluster L1
B
Endothelial
Fibroblast
Mesothelial
Myeloid
T
TEC
VSMC
CD4
CD8A
FOXP3
PDCD1
CXCR5
CXCL13
CD74
PECAM1
FN1
CLDN4
PSMB11
LAMP3
GABRA5
RYR3
ASC
B_GC
B_Naive
B_SM
B_USM
CD4_Naive
CD4_Tcm_Th0
CD4_Tcm_Th0act
CD4_Tcm_Th17
CD4_Tem_Th1
CD4_Temra
CD4_Tfh
CD4_Tfh_CXCL13
CD8_Naive
CD8_Tcm_Th0act
CD8_Tem
CD8_Tem_CXCL13
CD8_Temra
CD8_aa_I
CD8_aa_II
CyclingDNDP
DN
DP
Endothelial
Fibroblast_CLU
Fibroblast_CXCL12
ILC
Macrophage
Macrophage_NLRP3
Mesothelial
Monocyte_CD14
Monocyte_FCGR3A
NK
Treg_Eff
Treg_Naive
VSMC
cDC1
cDC2
cTEC
mTEC_AIRE
mTEC_CH3L1
mTEC_CHGA
mTEC_FEZF2
mTEC_GNB3
mTEC_KRT14
mTEC_KRT17
mTEC_POU2F3
migDC
nmTEC
pDC
Fraction of cells in group (%)
20 60 100
Mean expression in group
0 5
B
nmTEC
cTEC
mTEC_KRT14
Mesothelial
Doublet
mTEC_GNB3
mTEC_CH3L1
mTEC_KRT17
mTEC_FEZF2
mTEC_POU2F3
mTEC_AIRE
mTEC_CHGA
Fraction of cells in group (%)
20 60 100
log fold change
−5 0 5
C
Fibroblast_CLU
Fibroblast_CXCL12
VSMC
Fraction of cells in group (%)
20 60100
log fold change
−5 0 5
D
CD4_Tcm_Th0
CD4_Naive
CD8_Naive
CD8_aa_II
CD8_aa_I
DP
CD4_Tcm_Th17
CD4_Tem_Th1
CD4_Temra
CD8_Temra
NK
CD8_Tem
CD8_Tem_CXCL13
CD4_Tfh_CXCL13
Treg_Eff
Treg_Naive
CD8_Tcm_Th0act
CD4_Tcm_Th0act
CD4_Tfh
Doublet
ILC
Fraction of cells in group (%)
20 60100
log fold change
−5 0 5
E
B_Naive
B_SM
B_USM
ASC
B_GC
Doublet
Fraction of cells in group (%)
20 60100
log fold change
−5 0 5
F
Macrophage
Macrophage_NLRP3
Monocyte_CD14
Monocyte_FCGR3A
cDC1
cDC2
pDC
Doublet
migDC
Fraction of cells in group (%)
20 60100
log fold change
−5 0 5
G
CCR7
LAMP3
CD274
CD80
Doublet
Macrophage
Macrophage_NLRP3
Monocyte_CD14
Monocyte_FCGR3A
cDC1
cDC2
migDC
pDC
Fraction of cells in group (%)
20 60 100
Mean expression in group
0 2

Figure S5

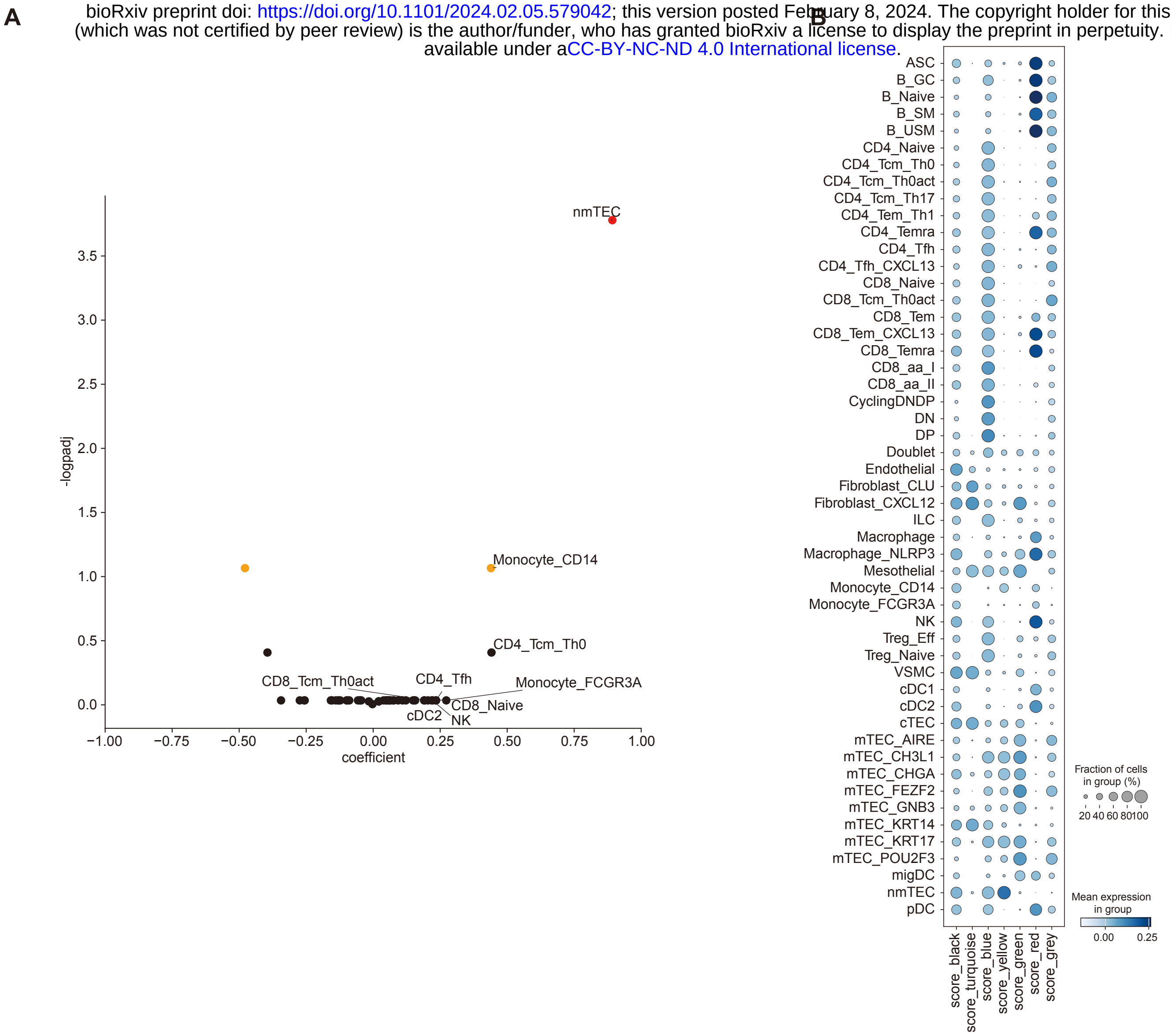
A
B
nmTEC
Monocyte_CD14
CD4_Tcm_Th0
CD8_Tcm_Th0act
CD4_Tfh
Monocyte_FCGR3A
CD8_Naive
cDC2
NK
-logpadj
coefficient
3.5
3.0
2.5
2.0
1.5
1.0
0.5
0.0
−1.00
−0.75
−0.50
−0.25
0.00
0.25
0.50
0.75
1.00
ASC
B_GC
B_Naive
B_SM
B_USM
CD4_Naive
CD4_Tcm_Th0
CD4_Tcm_Th0act
CD4_Tcm_Th17
CD4_Tem_Th1
CD4_Temra
CD4_Tfh
CD4_Tfh_CXCL13
CD8_Naive
CD8_Tcm_Th0act
CD8_Tem
CD8_Tem_CXCL13
CD8_Temra
CD8_aa_I
CD8_aa_II
CyclingDNDP
DN
DP
Doublet
Endothelial
Fibroblast_CLU
Fibroblast_CXCL12
ILC
Macrophage
Macrophage_NLRP3
Mesothelial
Monocyte_CD14
Monocyte_FCGR3A
NK
Treg_Eff
Treg_Naive
VSMC
cDC1
cDC2
cTEC
mTEC_AIRE
mTEC_CH3L1
mTEC_CHGA
mTEC_FEZF2
mTEC_GNB3
mTEC_KRT14
mTEC_KRT17
mTEC_POU2F3
migDC
nmTEC
pDC
score_black
score_turquoise
score_blue
score_yellow
score_green
score_red
score_grey
Fraction of cells
in group (%)
20 40 60 80 100
Mean expression
in group
0.00
0.25

Figure S6

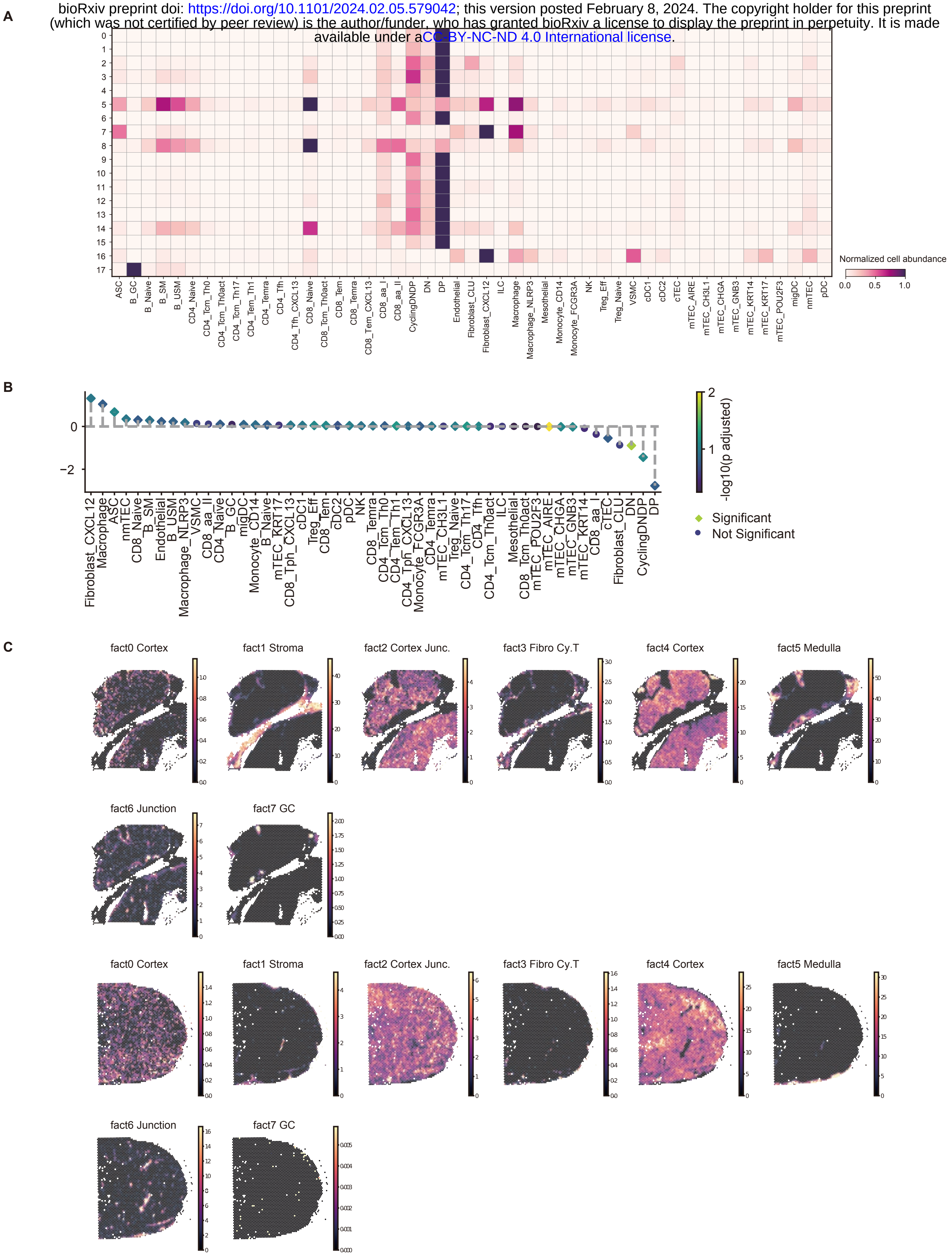
A
0 1 2 3 4 5 6 7 8 9 10 11 12 13 14 15 16 17
ASC
B_GC
B_Naive
B_SM
B_USM
CD4_Naive
CD4_Tcm_Th0
CD4_Tcm_Th0act
CD4_Tcm_Th17
CD4_Tem_Th1
CD4_Temra
CD4_Tfh
CD4_Tfh_CXCL13
CD8_Naive
CD8_Tcm_Th0act
CD8_Tem
CD8_Temra
CD8_Tem_CXCL13
CD8_aa_I
CD8_aa_II
CyclingDNDP
DN
DP
Endothelial
Fibroblast_CLU
Fibroblast_CXCL12
ILC
Macrophage
Macrophage_NLRP3
Mesothelial
Monocyte_CD14
Monocyte_FCGR3A
NK
Treg_Eff
Treg_Naive
VSMC
cDC1
cDC2
cTEC
mTEC_AIRE
mTEC_CH3L1
mTEC_CHGA
mTEC_GNB3
mTEC_KRT14
mTEC_KRT17
mTEC_POU2F3
migDC
nmTEC
pDC
Normalized cell abundance
0.0 0.5 1.0
B
0
−2
Fibroblast_CXCL12
Macrophage
ASC
nmTEC
CD8_Naive
B_SM
Endothelial
B_USM
Macrophage_NLRP3
VSMC
CD8_aa_II
CD4_Naive
B_GC
migDC
Monocyte_CD14
B_Naive
mTEC_KRT17
CD8_Tph_CXCL13
cDC1
Treg_Eff
CD8_Tem
cDC2
pDC
NK
CD8_Temra
CD4_Tcm_Th0
CD4_Tem_Th1
CD4_Tph_CXCL13
Monocyte_FCGR3A
CD4_Temra
mTEC_CH3L1
Treg_Naive
CD4_Tcm_Th17
CD4_Tfh
CD4_Tcm_Th0act
ILC
Mesothelial
CD8_Tcm_Th0act
mTEC_POU2F3
mTEC_AIRE
mTEC_CHGA
mTEC_GNB3
mTEC_KRT14
CD8_aa_I
cTEC
Fibroblast_CLU
DN
CyclingDNDP
DP
2
1
-log10(p adjusted)
Significant
Not Significant
C
fact0 Cortex
fact1 Stroma
fact2 Cortex Junc.
fact3 Fibro Cy.T
fact4 Cortex
fact5 Medulla
fact6 Junction
fact7 GC
fact0 Cortex
fact1 Stroma
fact2 Cortex Junc.
fact3 Fibro Cy.T
fact4 Cortex
fact5 Medulla
fact6 Junction
fact7 GC

Figure S7

A

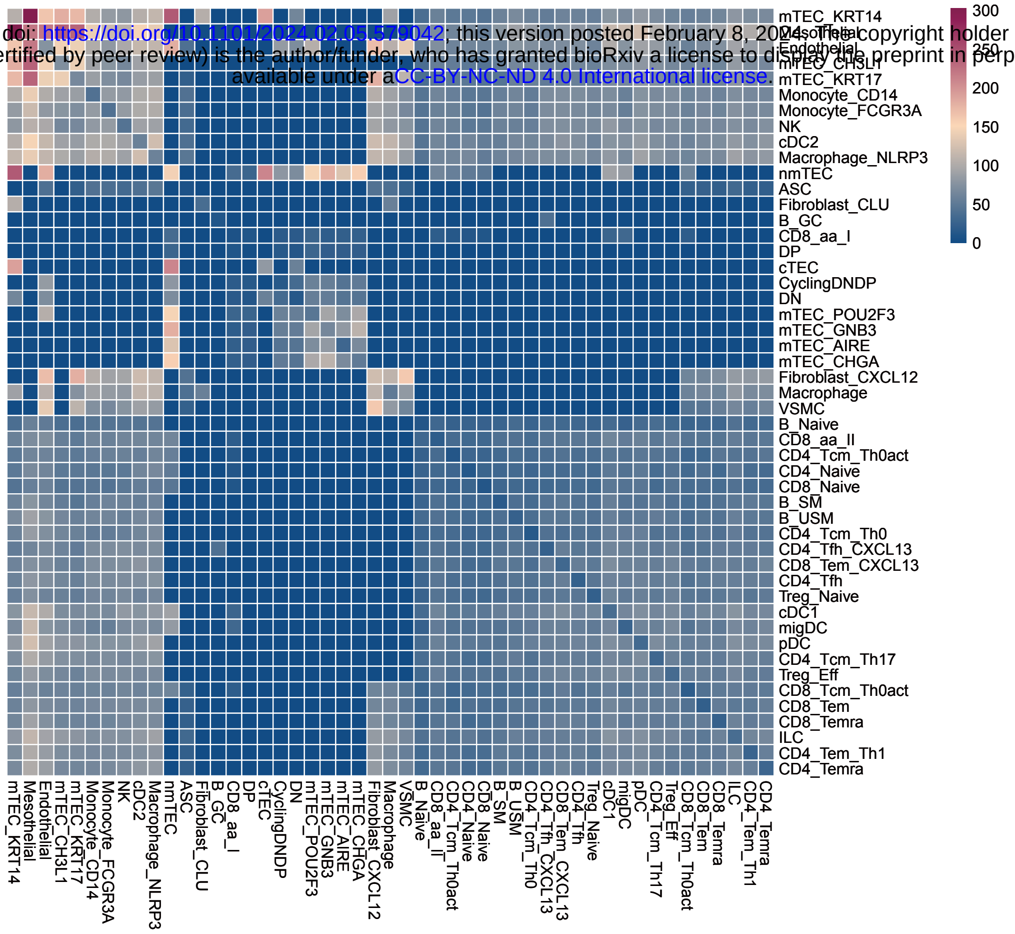
300
250
200
150
100
50
0
mTEC_KRT14
Mesothelial
Endothelial
mTEC_CH3L1
mTEC_KRT17
Monocyte_CD14
Monocyte_FCGR3A
NK
cDC2
Macrophage_NLRP3
nmTEC
ASC
Fibroblast_CLU
B_GC
CD8_aa_I
DP
cTEC
CyclingDNDP
DN
mTEC_POU2F3
mTEC_GNB3
mTEC_AIRE
mTEC_CHGA
Fibroblast_CXCL12
Macrophage
VSMC
B_Naive
CD8_aa_II
CD4_Tcm_Th0act
CD4_Naive
CD8_Naive
B_SM
B_USM
CD4_Tcm_Th0
CD4_Tfh_CXCL13
CD8_Tem_CXCL13
CD4_Tfh
Treg_Naive
cDC1
migDC
pDC
CD4_Tcm_Th17
Treg_Eff
CD8_Tcm_Th0act
CD8_Tem
CD8_Temra
ILC
CD4_Tem_Th1
CD4_Temra

B

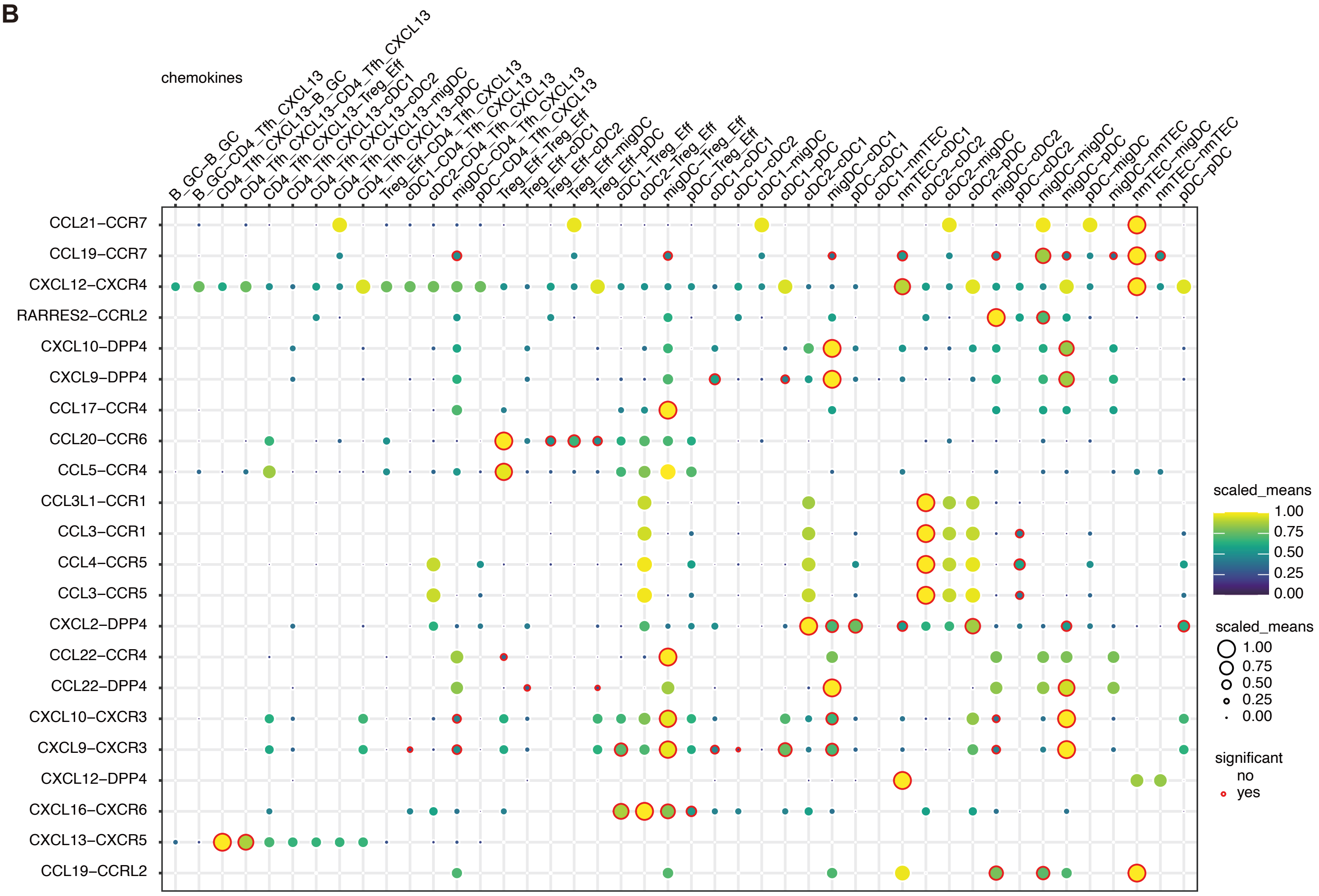
chemokines
B_GC–B_GC
B_GC–CD4_Tfh_CXCL13
CD4_Tfh_CXCL13–B_GC
CD4_Tfh_CXCL13–CD4_Tfh_CXCL13
CD4_Tfh_CXCL13–Treg_Eff
CD4_Tfh_CXCL13–cDC1
CD4_Tfh_CXCL13–cDC2
CD4_Tfh_CXCL13–migDC
CD4_Tfh_CXCL13–pDC
Treg_Eff–CD4_Tfh_CXCL13
cDC1–CD4_Tfh_CXCL13
cDC2–CD4_Tfh_CXCL13
migDC–CD4_Tfh_CXCL13
pDC–CD4_Tfh_CXCL13
Treg_Eff–Treg_Eff
Treg_Eff–cDC1
Treg_Eff–cDC2
Treg_Eff–migDC
Treg_Eff–pDC
cDC1–Treg_Eff
cDC2–Treg_Eff
migDC–Treg_Eff
pDC–Treg_Eff
cDC1–cDC1
cDC1–cDC2
cDC1–migDC
cDC1–pDC
cDC2–cDC1
migDC–cDC1
pDC–cDC1
cDC1–nmTEC
nmTEC–cDC1
cDC2–cDC2
cDC2–migDC
cDC2–pDC
migDC–cDC2
pDC–cDC2
migDC–migDC
migDC–pDC
pDC–migDC
migDC–nmTEC
nmTEC–migDC
nmTEC–nmTEC
pDC–pDC
CCL21–CCR7
CCL19–CCR7
CXCL12–CXCR4
RARRES2–CCRL2
CXCL10–DPP4
CXCL9–DPP4
CCL17–CCR4
CCL20–CCR6
CCL5–CCR4
CCL3L1–CCR1
CCL3–CCR1
CCL4–CCR5
CCL3–CCR5
CXCL2–DPP4
CCL22–CCR4
CCL22–DPP4
CXCL10–CXCR3
CXCL9–CXCR3
CXCL12–DPP4
CXCL16–CXCR6
CXCL13–CXCR5
CCL19–CCRL2
scaled_means
1.00
0.75
0.50
0.25
0.00
scaled_means
1.00
0.75
0.50
0.25
0.00
significant
no
yes

Figure S8

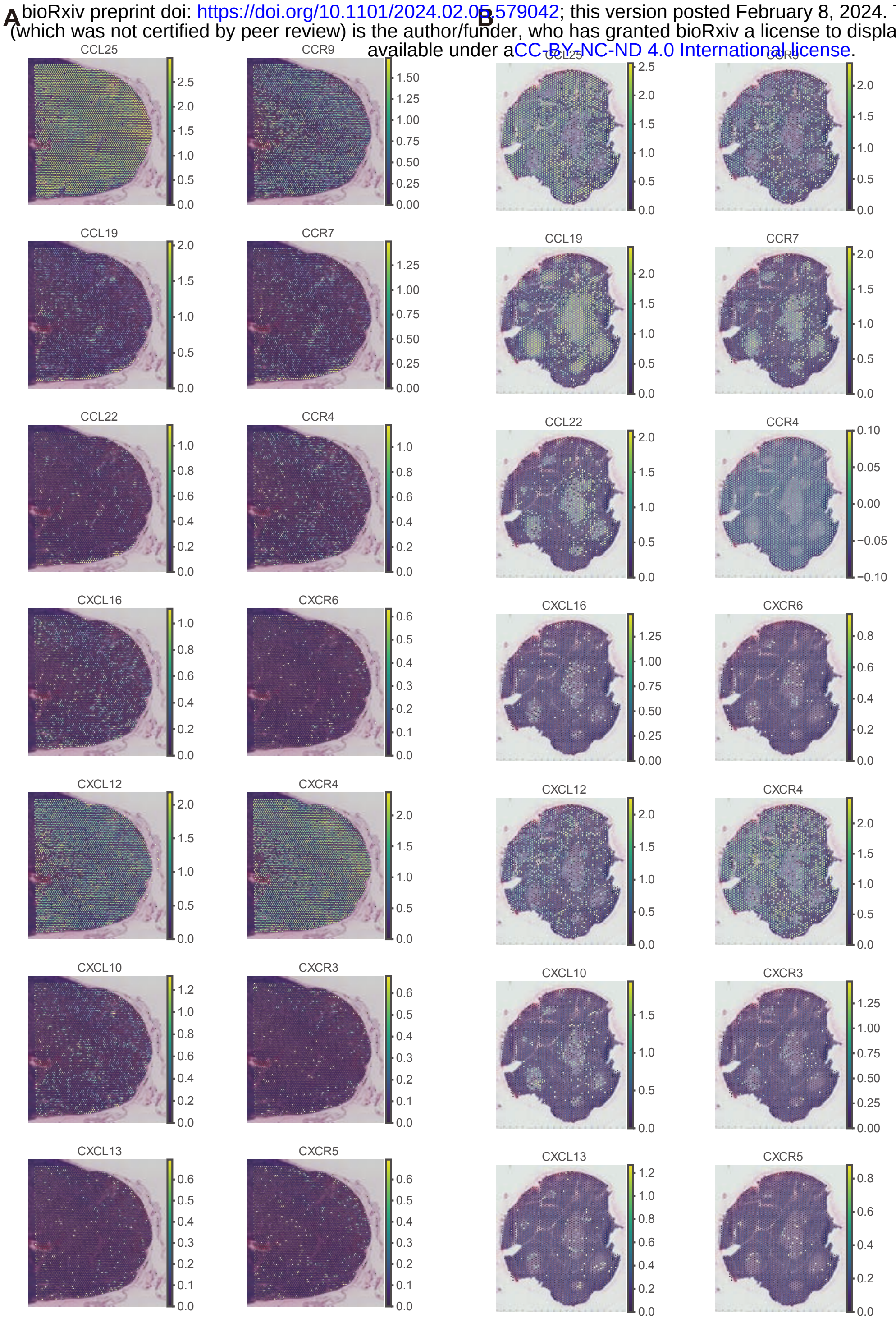
A
CCL25
2.5
2.0
1.5
1.0
0.5
0.0
CCR9
1.50
1.25
1.00
0.75
0.50
0.25
0.00
CCL19
2.0
1.5
1.0
0.5
0.0
CCR7
1.25
1.00
0.75
0.50
0.25
0.00
CCL22
1.0
0.8
0.6
0.4
0.2
0.0
CCR4
1.0
0.8
0.6
0.4
0.2
0.0
CXCL16
1.0
0.8
0.6
0.4
0.2
0.0
CXCR6
0.6
0.5
0.4
0.3
0.2
0.1
0.0
CXCL12
2.0
1.5
1.0
0.5
0.0
CXCR4
2.0
1.5
1.0
0.5
0.0
CXCL10
1.2
1.0
0.8
0.6
0.4
0.2
0.0
CXCR3
0.6
0.5
0.4
0.3
0.2
0.1
0.0
CXCL13
0.6
0.5
0.4
0.3
0.2
0.1
0.0
CXCR5
0.6
0.5
0.4
0.3
0.2
0.1
0.0
B
CCL25
2.5
2.0
1.5
1.0
0.5
0.0
CCR9
2.0
1.5
1.0
0.5
0.0
CCL19
2.0
1.5
1.0
0.5
0.0
CCR7
2.0
1.5
1.0
0.5
0.0
CCL22
2.0
1.5
1.0
0.5
0.0
CCR4
0.10
0.05
0.00
−0.05
−0.10
CXCL16
1.25
1.00
0.75
0.50
0.25
0.00
CXCR6
0.8
0.6
0.4
0.2
0.0
CXCL12
2.0
1.5
1.0
0.5
0.0
CXCR4
2.0
1.5
1.0
0.5
0.0
CXCL10
1.5
1.0
0.5
0.0
CXCR3
1.25
1.00
0.75
0.50
0.25
0.00
CXCL13
1.2
1.0
0.8
0.6
0.4
0.2
0.0
CXCR5
0.8
0.6
0.4
0.2
0.0

Figure S9

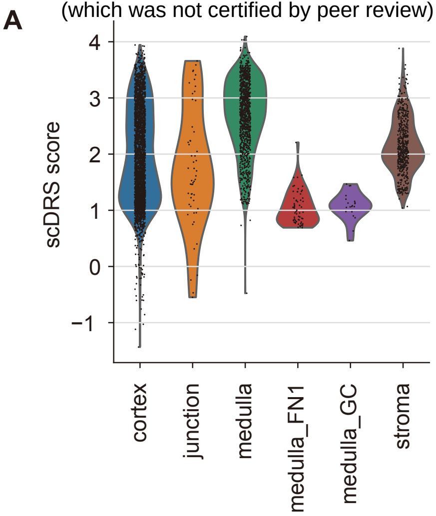
A
scDRS score
4
3
2
1
0
−1
cortex
junction
medulla
medulla_FN1
medulla_GC
stroma

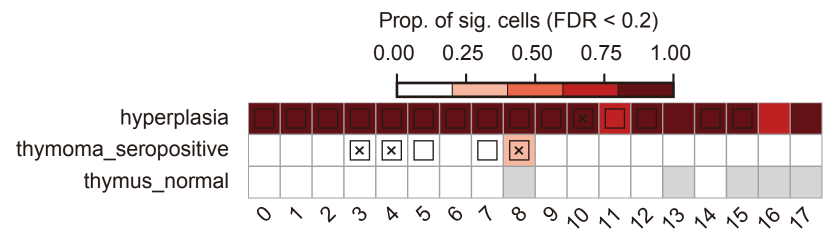
B
Prop. of sig. cells (FDR < 0.2)
0.00
0.25
0.50
0.75
1.00
hyperplasia
thymoma_seropositive
thymus_normal
0
1
2
3
4
5
6
7
8
9
10
11
12
13
14
15
16
17